Received: 22 November 2019 | Revised: 9 January 2020 | Accepted: 22 January 2020

DOI: 10.1111/gbi.12385

ORIGINAL ARTICLE

gebiology WILEY

In Situ Fe and S isotope analyses in pyrite from the 3.2 Ga Mendon Formation (Barberton Greenstone Belt, South Africa): Evidence for early microbial iron reduction

Johanna Marin-Carbonne[1,2] | Vincent Busigny[3,4] | Jennyfer Miot[5] | Claire Rollion-Bard[3] | Elodie Muller[3] | Nadja Drabon[6] | Damien Jacob[7] | Sylvain Pont[5] | Martin Robyr[2] | Tomaso R. R. Bontognali[8,9] | Camille François[10] | Stephanie Reynaud[11] | Mark Van Zuilen[3] | Pascal Philippot[3,12]

[1]Univ Lyon, UJM Saint Etienne, UCA, CNRS, IRD, UMR 6524, Laboratoire Magma et Volcans, Saint Etienne, France

[2]Institut des Sciences de la Terre, Université de Lausanne, Lausanne, Switzerland

[3]Université de Paris, Institut de Physique du Globe, CNRS, Paris, France

[4]Institut Universitaire de France, Paris, France

[5]Institut de Minéralogie, Physique des Matériaux et Cosmochimie (IMPMC), Muséum National d'Histoire Naturelle, Centre National de la Recherche Scientifique UMR 7590, IRD 206, Université Pierre et Marie Curie, Sorbonne Universités, Paris, France

[6]Department of Geological Sciences, Stanford University, Stanford, CA, USA

[7]UMET UMR 8207 CNRS, Université de Lille, Villeneuve d'Ascq, France

[8]Space Exploration Institute, Neuchâtel, Switzerland

[9]Department of Environmental Sciences, University of Basel, Basel, Switzerland

[10]Early Life Traces & Evolution-Astrobiology Lab, Department of Geology, B18, University of Liege, Liège, Belgium

[11]Laboratoire Hubert Curien, CNRS, Univ Lyon, UJM Saint Etienne, Saint Etienne, France

[12]Géosciences Montpellier, CNRS-UMR 5243, Université de Montpellier, Montpellier, France

Correspondence
Johanna Marin-Carbonne, Laboratoire Magma et Volcans, UCA, CNRS, Univ Lyon, UJM Saint Etienne, IRD 23 rue Paul Michelon, 42100 St Etienne, France.
Email: johanna.marincarbonne@unil.ch

Funding information
The SEM facility at IMPMC is supported by Région Ile de France grant SESAME 2006 N°I-07-593/R, INSU/CNRS, UPMC-Paris 6, and Agence Nationale de la Recherche (ANR grand No. ANR-07-BLAN-0124-01). The TEM facility at IMPMC is supported by Région Ile de France grant SESAME 2000 E 1435. The TEM national facility in Lille (France) is supported by the Conseil Regional du Nord-Pas de Calais, the European Regional Development Fund (ERDF), and the Institut National des Sciences de l'Univers (INSU, CNRS). This research was supported by the Labex UnivEarths program of Sorbonne Paris Cité (ANR-10-LABX-0023

Abstract

On the basis of phylogenetic studies and laboratory cultures, it has been proposed that the ability of microbes to metabolize iron has emerged prior to the Archaea/Bacteria split. However, no unambiguous geochemical data supporting this claim have been put forward in rocks older than 2.7–2.5 giga years (Gyr). In the present work, we report in situ Fe and S isotope composition of pyrite from 3.28- to 3.26-Gyr-old cherts from the upper Mendon Formation, South Africa. We identified three populations of microscopic pyrites showing a wide range of Fe isotope compositions, which cluster around two δ^{56}Fe values of −1.8‰ and +1‰. These three pyrite groups can also be distinguished based on the pyrite crystallinity and the S isotope mass-independent signatures. One pyrite group displays poorly crystallized pyrite minerals with positive Δ^{33}S values > +3‰, while the other groups display more variable and closer to 0‰ Δ^{33}S values with recrystallized pyrite rims. It is worth to note that all the pyrite groups display positive Δ^{33}S values in the pyrite core and similar trace element compositions.

and ANR-11-IDEX-0005-02), the INSU Programme National de Planétologie and the ANR (project SRB – ANR-14-CE33-0003-01 to JM). VB thanks the IUF. JMC thanks the Laboratory of Excellence initiative (n°ANR-10-LABX-0006), the Région Auvergne, the European Regional Development Fund and the European Research Council (ERC) under the European Union's Horizon H2020 research and innovation program (STROMATA, grant agreement 759289). P.P. acknowledges support from the São Paulo Research Foundation (FAPESP grant 2015/16235-2).

We therefore suggest that two of the pyrite groups have experienced late fluid circulations that have led to partial recrystallization and dilution of S isotope mass-independent signature but not modification of the Fe isotope record. Considering the mineralogy and geochemistry of the pyrites and associated organic material, we conclude that this iron isotope systematic derives from microbial respiration of iron oxides during early diagenesis. Our data extend the geological record of dissimilatory iron reduction (DIR) back more than 560 million years (Myr) and confirm that microorganisms closely related to the last common ancestor had the ability to reduce Fe(III).

KEYWORDS

Archean, Barberton Greenstone Belt, dissimilatory Iron reduction, iron and Fe isotopes, Mendon cherts, SIMS

1 | INTRODUCTION

The identification of early traces of life in the geological record is challenging due to the scarcity and complex post-depositional history of early Archean rocks. Given their micrometer size and chemical composition (dominated by organic molecules prone to oxidation), the first forms of life, Archaea and Bacteria, did not leave unambiguous fossils (Brasier, Green, Lindsay, & Steele, 2004 cf.; Schopf, Kudryavtsev, Czaja, & Tripathi, 2007). Biominerals associated with residual organic matter are among the best evidence of ancient microbial activity (Brasier et al., 2004; Schopf et al., 2007). Pyrite (FeS_2) is one of them and can be found in some of the oldest sedimentary rocks on earth. Pyrite has been extensively studied for reconstructing past environmental conditions of the early earth, especially atmospheric composition. Since the canonical work of Farquhar and colleagues and the discovery of mass-independent fractionated sulfur (S-MIF) isotope signatures in Archean pyrite (Farquhar, Bao, & Thiemens, 2000), it is well established that Archean pyrites record atmospheric sulfur cycle. S-MIF signatures are expressed as $\Delta^{33}S$, a deviation from a mass-dependent fractionation relationship, which can be expressed as (Farquhar et al., 2000; Ono, Wing, Johnston, Farquhar, & Rumble, 2006) follows:

$$\Delta^{33}S = \delta^{33}S - \left(\left(1+\delta^{34}S/1000\right)^{0.5152} - 1\right) \times 1000$$

where $\delta^{x}S = (({}^{x}S/{}^{32}S)_{sample}/({}^{x}S/{}^{32}S)_{reference} - 1) \times 1{,}000$ (‰) (x = 33, and 34) and the reference is Canyon Diablo Troilite (V-CDT, Ding et al., 2001). Photochemical reactions of dissociation of volcanic SO_2 in an anoxic atmosphere can produce both elemental sulfur and sulfate aerosols with positive and negative $\Delta^{33}S$ values, respectively. Although alternative views exist (Oduro et al., 2011), it is generally acknowledged that O_2 levels below 10^{-5} present atmospheric level (PAL) are critical for the production and preservation of S-MIF in the geological record (Farquhar et al., 2000; Harman, Pavlov, Babikov, & Kasting, 2018; Thiemens & Lin, 2019; Ueno, Ono, Rumble, & Maruyama, 2008; Zhelezinskaia, Kaufman, Farquhar, & Cliff, 2014). Both photochemical experiments and studies of sedimentary sulfides and sulfate have then confirmed that Archean sulfate has negative $\Delta^{33}S$ values while elementary sulfur has positive $\Delta^{33}S$ values (Endo, Danielache, & Ueno, 2019; Farquhar et al., 2000; Farquhar, Wu, Canfield, & Oduro, 2010; Halevy, 2013; Harman et al., 2018; Muller et al., 2017; Ueno et al., 2008; Zhelezinskaia et al., 2014). Sulfur in archean sedimentary pyrite may predominantly originate either from a sulfate-derived sulfide pool (e.g., following microbial sulfate reduction) or from an elemental sulfur derived pool of polysulfides that may further react with iron sulfide precursors (Farquhar et al., 2013). Indeed diagenetic pyrite formation pathways are complex and involve various precursors either molecular (including elemental sulfur and polysulfides) or mineral (including FeS mackinawite and Fe_3S_4 greigite; Rickard, 2012). Reconciliating S and Fe isotope compositions of sulfide with their precise diagenetic pathway is still complex as some large isotopic discrepancies between pyrite mineral and the porewater composition have been observed in modern environments (Gomes, Fike, Bergmann, Jones, & Knoll, 2018; Raven, Sessions, Fischer, & Adkins, 2016). However, it is well established that sedimentary pyrite can record past microbial metabolisms (Fike, Bradley, & Rose, 2015). While pyrite may form secondarily during late diagenesis or metamorphism following abiotic pathways, several microbial metabolisms have also been proposed to be involved in the formation of early diagenetic pyrite. These include bacterial sulfate reduction, sulfur reduction and disproportionation, and dissimilatory iron reduction (Rickard, 2012). These various metabolic processes can potentially be traced and distinguished from abiotic routes using iron and sulfur isotope compositions recorded in pyrite (Beard et al., 1999; Canfield, 2001; Johnson, Beard, & Roden, 2008; Johnston, 2011).

For instance, the oldest traces of bacterial sulfate reduction and sulfur disproportionation were evidenced from S isotope composition of pyrite in 3.47-Gyr-old barite deposits from North Pole, Australia (Philippot et al., 2007; Shen, Buick, & Canfield, 2001). Microbial dissimilatory iron reduction (DIR, a form of respiration where ferric iron is used as an electron acceptor) also plays a role in Fe sulfide formation as it promotes the reduction in ferric iron minerals into dissolved ferrous iron, which can then react with dissolved sulfide to precipitate mackinawite (FeS), a key precursor of pyrite (Rickard, 2012). DIR imparts a strong Fe isotope fractionation, enriching the product in the light isotope by ~3‰ (Crosby, Roden, Johnson, & Beard, 2007).

This light Fe isotope signature was previously used as a proxy of DIR in Archean rocks as old as 2.7–2.5 Gyr (Archer & Vance, 2006; Czaja et al., 2010; Heimann et al., 2010; Johnson, Ludois, Beard, Beukes, & Heimann, 2013; Nishizawa, Maruyama, Urabe, Takahata, & Sano, 2010) and even as old as 3.8 Gyr (Craddock & Dauphas, 2011; Czaja et al., 2013). However, because an unambiguous interpretation of the 3.8 Gyr signals is hampered by the strong metamorphism experienced by early Archean rocks (Ueno, Yurimoto, Yoshioka, Komiya, & Maruyama, 2002), the Fe isotope signature recorded in 2.7 Gyr sediments can be considered as the earliest firm evidence for DIR (Czaja et al., 2013). Consistently, DIR may have evolved only after the spread of oxygen photosynthesis (Czaja et al., 2013).

In the present work, we analyzed both Fe and S isotope compositions of individual pyrite crystals in 3.28–3.26 Gyr sedimentary rocks from the well-preserved Mendon Formation (South Africa). Together with high-resolution mineralogy and trace element concentrations, the data are used to constrain the mechanisms of pyrite formation and evaluate in particular the impact of diagenesis and metamorphism on pyrite composition.

2 | SAMPLES AND METHODS

2.1 | Geological context and samples description

The 3.6–3.2 Ga Barberton Greenstone Belt is located in the east of the Kaapvaal Craton, South Africa. It consists of mafic, ultramafic, and felsic volcanic rocks alternating with sedimentary successions, termed the Swaziland Supergroup. Three main lithostratigraphic units compose the Swaziland Supergroup. These are the Onverwacht Group, the Fig Tree Group, and the Moodies Group, in ascending stratigraphic order (Lowe & Byerly, 2007; Viljoen & Viljoen, 1970).

The 3550- to 3260-Myr-old Onverwacht Group (Kröner, Hegner, Wendt, & Byerly, 1996) is composed of six units: Sandspruit, Theespruit, Komati, Hooggenoeg, Kromberg, and Mendon Formations (Lowe & Byerly, 1999). The Sandpruit, Theespruit, Hooggenoeg, and Kromberg Formations consist of basaltic, komatiitic, and felsic volcanic rocks and minor cherts. The Komati and Mendon Formations are composed mainly of komatiites and minor cherts. The central greenstone belt has been metamorphosed in greenschist facies conditions (i.e., ~350°C; Tice, Bostick, & Lowe, 2004). The Fig Tree and Moodies Groups consist of sandstone, shale, chert, banded iron formation, and felsic volcanic rocks, which have been dated at ca. 3,280–3,216 Myr (Byerly, Kröner, Lowe, Todt, & Walsh, 1996; Drabon, Galić, Mason, & Lowe, 2019; Hofmann, 2005; Kamo & Davis, 1994; Kröner et al., 1996; de Ronde, Wit, & Spooner, 1994).

The samples analyzed in this study come from the Barberton Drilling Project (BBDP2) drill core (Figure 1), located at 25°54′24.8″S and 31°03′23.9″E, hole azimuth 288° and dip 50° (Philippot et al., 2009). About 100 m of the uppermost Mendon Formation was recovered. The Mendon Formation was deposited between 3.34 and 3.26 Gyr and has been studied in detail (Busigny et al., 2017; Galić et al., 2016; Hofmann & Bolhar, 2007; Lowe & Byerly, 1999; Montinaro et al., 2015; Philippot et al., 2009; Philippot, Zuilen, & Rollion-Bard, 2012; Tice et al., 2004; Trower & Lowe, 2016). The sequence consists of five volcanic cycles, termed Mv1 through Mv5, which are each capped by thin chert sequences, termed Mc1 through Mc5 (Byerly et al., 1996). In the BBDP2 drill core, the Mendon Formation is composed of volcanic rocks, mostly komatiite and silicified komatiite of the Mv5 cycle, which are overlain by ~60 m of finely laminated cherts of the Mc5 cycle (Decker, Byerly, Stiegler, Lowe, & Stefurak, 2015). The base of the Mc5 sequence was dated at 3.28 Gyr, and the top is marked by the S2 spherule layer that was deposited at 3.26 Gyr (Decker et al., 2015). Mc5 corresponds to a wide variety of chert, with mostly black chert and ferruginous gray chert, and minor amounts of black and white banded chert, banded ferruginous chert, intraclast breccia and silicified green colored ash and accretionary lapilli (Trower & Lowe, 2016). The Mendon Formation was deposited during a period of local volcanic quiescence with slow sedimentation rates under quiet water settings (Lowe & Byerly, 1999; Trower & Lowe, 2016).

Twelve samples were selected based on sulfide abundance; their name indicates the location (in meter) along the drill core (Table 1). Most samples correspond to black cherts composed of microcrystalline quartz and minor amounts of organic matter and iron carbonates (Figure 2 and Table 1). The size of disseminated pyrites varies over a large range from 10 μm to 1 cm (Figure 2 and Table 1). The chert samples were affected by late fluid circulation, as illustrated by the presence of numerous quartz, carbonates, and chlorite veins linked to regional metamorphism (Busigny et al., 2017). However, primary sedimentary structures are well-preserved, with fine laminations, especially in samples 114.30 and 114.33, which have experienced only limited fluid circulation overprint (Figure 2 and Table 1). Alteration phases are present as ganterite (barium-rich mica), chlorite, and fuchsite. Minor phases of barite, iron oxide, nickel-rich iron oxide, and rutile are also present. Sulfides occur essentially as pyrite, but one sample (94.92) shows the presence of chalcopyrite and pentlandite. One sample (160.12) represents altered komatiites in which spinifex texture has been preserved, with olivine pseudomorphed by ankerite, dolomite, quartz, fuchsite, ganterite, and small grains of barite (Figure 2). Sample 160.12 displays large (mm) pyrites and smaller (>100 μm) cubic pyrites. Sample 147.38 contains one large (mm) square pyrite with visible mineral (quartz and ankerite) inclusions (Figure 2). Very small pyrites (<10 μm) are present in the chert matrix but were not studied here due to their small size compared with ion microprobe beam size.

2.2 | Methods

2.2.1 | SEM and TEM analyses

Scanning electron microscopy (SEM) and energy-dispersive X-ray spectrometry (EDS) were used to characterize the microstructure and chemistry of pyrite and its inside inclusions for subsequent in situ extraction using focused ion beam milling (FIB).

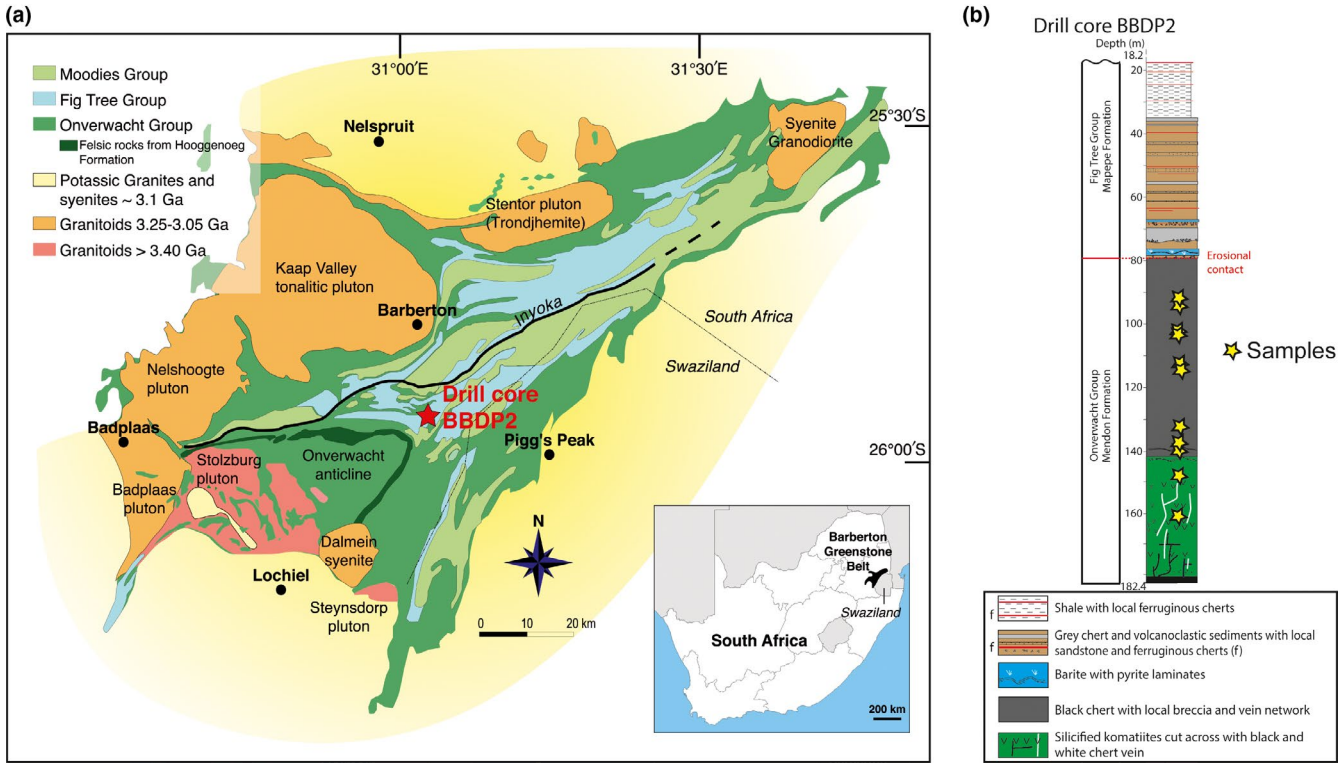

FIGURE 1 Geological map of the Barberton Greenstone Belt (from Busigny et al. 2017). The BBDP2 drill core is indicated by the red star and the samples location by yellow stars

TABLE 1 Mineralogical description of the Mendon chert samples

Depth	Rock description	Primary sedimentary features	Secondary veins	Pyrites			
				Morphology	Size (μm)	Inclusions	Group
94.92	Black chert	Yes	20%	Euhedral	100–200	Qz, sid, mica	B
95.41	Black chert	Yes	30%	Euhedral	100–300	Qz, mica, C org	B
104.80	Black chert	Yes	5%	Cubic	1,000	Qz, Ank, C org	A
104.83	Black chert	Yes	5%	Cubic	1,000	Qz, Ank, C org	A and B
114.30	Black chert	Yes	<5%	Aggregated	50–100	Qz, sid, C org.	C
114.33	Black chert	Yes	<5%	Aggregated	50–100	Qz, sid, C org	C
135.55	Black chert	No	50%	Euhedral	50–1,000	Qz, Ank	B
137.84	Black chert	Yes	5%	Euhedral	100– 1,000	Qz, sid	A
139.80	Black and white chert	Yes	5%	Euhedral	50–100	Qz	C
147.38	White chert	No	10%	Euhedral	1,000	Qz, Ank	B
160.12	Altered Komatiite	No	50%	Eudedral	100–300	Qz, Ank, mica, rutile	A and B

Note: Qz for quartz, sid for siderite, Ank for ankerite, and C org for organic matter.

SEM observations were performed on a TESCAN VEGAII LSU at IMPMC with 15 kV accelerating voltage and a working distance of 15.4 mm according to the geometrical conditions required for EDS analyses on this microscope. SEM images were collected with both secondary (SE) and backscattered electrons (BSE) detectors. FIB ultrathin sections were extracted from different pyrite grains using an FEI Strata DB 235 at IEMN (Lille, France Schiffbauer & Xiao, 2009; Wirth, 2009). This extraction procedure maintains textural integrity and prevents shrinkage and deformation of microscale to nanoscale pores, even in the case of highly sensitive materials (Bassim, Scott, & Giannuzzi, 2014).

Transmission electron microscopy (TEM) analyses were performed on FIB sections to characterize crystallographic orientation and textures of the pyrites. TEM observations were performed with

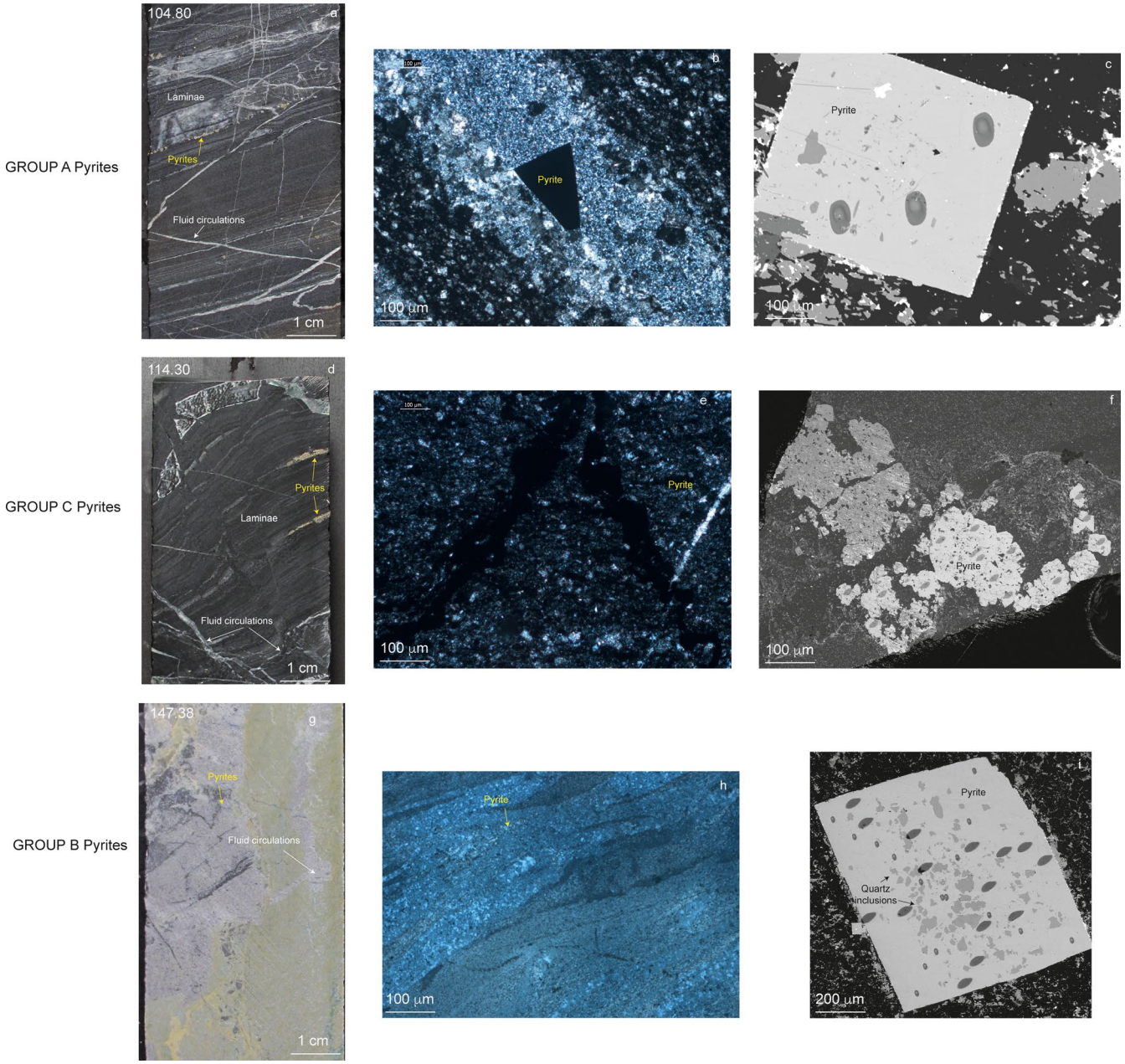

FIGURE 2 Petrography images of the three groups of pyrites. Images show an optical photograph of the core (a, d, g), an optical photomicrograph of the thin section of each sample (b, e, h), and a SEM picture of the analyzed pyrite (c, f, i). The group A pyrite is exemplified by sample 104.80, the group B by sample 147.38, and the group C by sample 114.30. The core pictures show the importance of fluid circulations identified as quartz veins. We can also note the presence of thin laminations, with a little less fluid circulations in the case of sample 114.30. It is also worth to note that the pyrites occur in proximity to these fluid circulations. All the samples consist of chert with a majority of microquartz; however, samples 104.80 and 147.38 contain also more iron carbonate (ankerite) than sample 114.30. These cherts are rich in organic matter visible in the darkness of the matrix. The pyrites display different shapes but are mostly cubic. The SIMS spots are still visible on the images as well as some leftover of the gold coating. All the pyrites display inclusions of quartz and occasionally of organic matter

JEOL 2100F field emission gun (FEG) microscopes (IMPMC—Paris, France, and IEMN—Lille, France) operating at 200 kV. Scanning transmission electron microscopy (STEM) Z-contrast imaging was performed using the high-angle annular dark field (HAADF) mode. High-resolution TEM (HRTEM) images were collected in the bright field mode. Selected-area diffraction (SAED) patterns were obtained on areas of interest.

2.2.2 | Trace element composition

The chemical composition of pyrite from 3 chert samples was investigated by Electron Probe Micro-Analyzer (EPMA) at UNIL. In large pyrite grains, EPMA traverses were performed to quantify the trace element content of pyrite using a 5 spectrometer-equipped JEOL JXA-8530F. The operational conditions were 15 kV acceleration potential

difference, 40 nA beam current, and a fully focused beam (<1 μm in diameter). A set of sulfides, silicates, oxides, and native elements, including FeS_2 (for Fe), CuS (for S and Cu), PbS (for Pb), ZnS (for Zn), Mn_2SiO_4 (for Mn), NiO (for Ni), and Co, was used as reference materials. All of the used reference materials were tested before the quantitative analysis. Elements and X-ray lines used for analysis were Fe (Kα), Co (Kα), Ni (Kα), Cu (Kα), Zn (Kα), S (Kα), Mn (Kα), and Pb (Mα). Detection limits were between 145 ppm by weight for Co, 160 ppm for Cu, 115 ppm for Mn, 700 ppm for Pb, 130 ppm for Mn, and 200 ppm for Zn on average. For each traverse, analysis spots were placed at 60 μm spacing.

2.2.3 | Carbon isotope analysis

Seven rock samples from the Mendon Formation were powdered to <60 μm using a ring and puck mill. Sample powders (about 1 g) were reacted with excess HCl (6 N) at room temperature in glass beakers during one night to remove carbonates. After removing the supernatant, samples were acidified again with HCl (6 N) at 80°C and agitated during 2 hr to guarantee full sample decarbonation. After decantation, the residues were rinsed with deionized distilled water until neutral, centrifuged, and dried at 60°C overnight. TOC content and $\delta^{13}C_{org}$ values were measured for carbonate-free residues with a Flash EA1112 elemental analyzer coupled to a Thermo Finnigan DELTA plus XP isotope ratio mass spectrometer interfaced with a ConFlo IV interface at the stable isotope laboratory of the Institut de Physique du Globe de Paris (IPGP). Our results were normalized using three internal standards with 5 different amounts, which were used to estimate the concentration of organic C (wt.%). Reproducibility on $\delta^{13}C_{org}$ and TOC measurements based on at least triplicate measurements of the samples is usually better than ±0.4‰ and ±0.01 wt.%, respectively (1σ).

2.2.4 | SIMS Fe and S isotopes analyses

Iron and sulfur isotopes are expressed in delta notation (δ^{56}Fe, δ^{34}S, and δ^{33}S) relative to the international standards IRMM-014 (for Fe) and V-CDT (for S) based on the following equation:

$$\delta^{i}X = \left[\left({}^{i}X/{}^{j}X_{sample}\right) / \left({}^{i}X/{}^{j}X_{standard}\right) - 1\right] \times 1000$$

where X is Fe or S, i and j represent the heavy and light isotopes, respectively (54 and 56 for Fe and 34 or 33 and 32 for S). Sulfur mass-independent fractionation has been calculated as the deviation from the Terrestrial Fractionation Line (TFL), using the mass discrimination law (Farquhar et al., 2000), where the factor 0.5152 defines the slope of the TFL.

Iron isotope compositions were measured with a Cameca ims 1270 ion microprobe at CRPG following the procedure described in Marin-Carbonne, Rollion-Bard, and Luais (2011). Briefly, a $^{16}O^-$ primary beam of 10–13 nA intensity was focused to a spot of about 15 μm diameter and less than 1 μm in depth. The mass resolution was set to ~7,000, and $^{54}Fe^+$ and $^{56}Fe^+$ were measured in multi-collection mode with two off-axis Faraday cups. Typical ^{56}Fe intensity was between 5 and 6 × 10^7 counts per second (cps). A typical analysis consisted of 2 min pre-sputtering followed by data acquisition in 30 cycles of 5 s acquisition time. The isobaric interference of ^{54}Cr on ^{54}Fe was corrected by monitoring chromium on masses 52, but chromium levels were negligible in all samples. The internal precision for δ^{56}Fe values was typically better than ±0.1‰ (2σ), and the external reproducibility based on multiple measurements of our pyrite reference material (Balmat with δ^{56}Fe = −0.399‰, (Whitehouse & Fedo, 2007)) was better than ±0.2‰ (2σ).

Sulfur isotope compositions were measured on the Cameca ims 1280 HR2 (CRPG) by simultaneous measurements of $^{32}S^-$, $^{33}S^-$, and $^{34}S^-$ in multi-collection mode with three Faraday cups. A Cs^+ primary beam of 5 nA intensity was focused to a spot of about 15–20 μm in diameter and less than 1 μm in depth. The mass resolution was set to 5,000 to resolve the isobaric interferences due to hydrides on sulfur isotopes. Typical $^{32}S^-$ intensity was between 6 and 10 × 10^8 counts per second (cps) depending on the sulfide mineral analyzed. A typical analysis consisted of 2 min of pre-sputtering followed by data acquisition in 30 cycles of 3 s each. The background of the detectors was measured during pre-sputtering and was then corrected for each analysis. Several pyrite standards Maine (δ^{34}S = −20.61‰, δ^{33}S = −10.63‰), Spain (δ^{34}S = −1.56‰ and δ^{33}S = −0.78‰), and Balmat (δ^{34}S = 15.84‰ and δ^{33}S = 8.12‰(Muller et al., 2017) were used to determine (a) the instrumental mass fractionation by considering the average value obtained on the three standards and (b) the reference mass discrimination line, from which Δ^{33}S values were calculated. The internal precision achieved under these conditions was better than ±0.05‰ for δ^{34}S and ±0.03‰ for δ^{33}S (2σ). The external precision was ±0.40‰ (2σ) for δ^{34}S and ±0.1‰ (2σ) for Δ^{33}S values.

3 | RESULTS

3.1 | SEM and TEM observations

Ultrathin sections of selected pyrites were characterized by secondary electron microscopy and transmission electron microscopy—in order to discriminate primary features from late modifications related to metamorphism and hydrothermal overprint (Figure 3). On the basis of high-resolution TEM and electron diffraction analyses, two different textures of pyrite were identified as exemplified with samples 114.30 and 147.38. Pyrites from sample 114.30 are composed of nanocrystals with various orientations embedded within a single large pyrite mineral (Figure 3a–c). Nanocrystals of pyrite support a very early diagenetic origin, consistent with the preservation of early diagenetic fine laminations. In contrast, pyrites present in sample 147.38 consist of homogeneous single crystals, typical for a post-diagenetic origin (metamorphic, hydrothermal) and indicating recrystallization features overprinting a primary texture (Figure 3d–f).

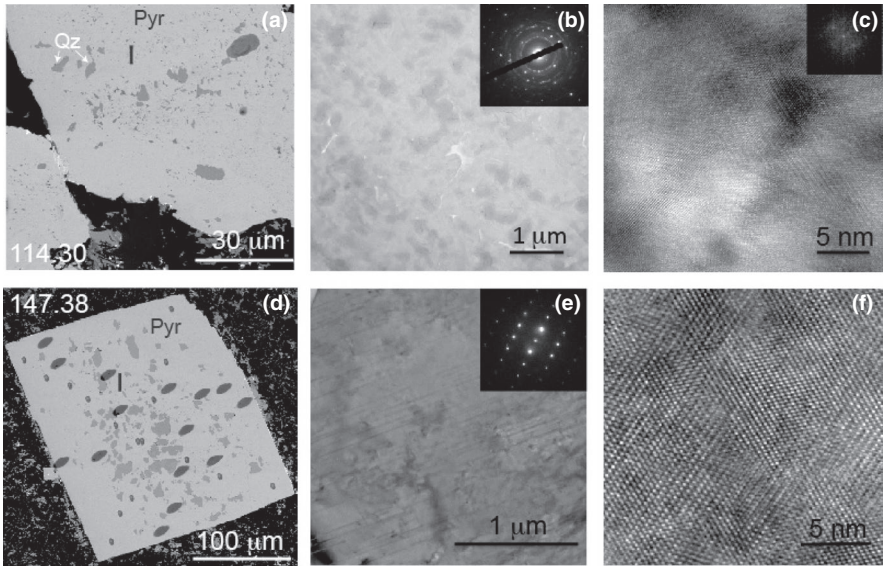

FIGURE 3 Pyrite microphotographs (SEM and TEM) and associated diffraction patterns for samples 114.30 (a, b, c) and 147.38 (d, e, f). SEM analyses (a, d) show quartz inclusions in pyrites, whereas the matrix is composed of microquartz, altered iron carbonate (ankerite), chlorite, and ganterite (Ba-rich mica) recovered by coating. Sample 114.30 contains disoriented nm-scale pyrite particles (see powder diffraction pattern in b and HRTEM image in c) embedded within a pyrite single crystal matrix (see superimposed electron diffraction pattern in b, (<10–2> zone axis) and FFT signal of the matrix in c, displaying the same zone axis). In contrast, for sample 147.38, electron diffraction analysis (e) and HRTEM (f) indicate that pyrite is present as large single crystals (<–113> zone axis). The black bar in (a) and (b) represents the location of the FIB ultrathin section

TABLE 2 Average trace element concentration (in ppm) of pyrite from Mendon Cherts

Pyrite group	Co (ppm)	Cu (ppm)	Mn (ppm)	Pb (ppm)	Ni (ppm)	Zn (ppm)
A	b.d.l.	408	b.d.l.	b.d.l.	434	b.d.l.
B	b.d.l.	b.d.l	b.d.l.	b.d.l.	1,750	b.d.l.
C	b.d.l.	b.d.l.	b.d.l.	b.d.l.	170	b.d.l.

Note: Detection limits between 145 ppm for Co, 160 ppm for Cu, 115 ppm for Mn, 700 ppm for Pb, 130 ppm for Ni, and 200 ppm for Zn.

Abbreviation: b.d.l., below detection limit.

TABLE 3 Total organic carbon (TOC, in wt.%) and C_{org} isotope composition of Mendon cherts ($\delta^{13}C$ vs. V-PDB, in ‰)

Pyrite group	Sample name	$\delta^{13}C$ (‰)	±1σ	TOC (wt%)	±1σ
A	104.80	−32.10	0.20	1.51	0.06
	104.83	−31.39	0.19	1.04	0.01
B	95.41	−30.20	0.08	0.38	0.02
	139.8	−28.36	0.16	0.27	0.03
	160.12	−26.56	1.40	0.03	0.03
C	114.3	−31.80	0.59	1.13	0.07
	144.33	−31.40	0.32	0.82	0.01

3.2 | Trace element composition of the pyrite

Various trace elements (Co, Ni, Cu, Zn, Pb, and Mn) have been analyzed by EPMA in 3 chert samples and are presented in Table 2. The average concentrations of trace elements are very low (<0.2 wt.%) and often below the detection limit, with for instance no detectable Co, Mn, Zn, and Pb. Each pyrite crystal shows limited internal variability, with no significant difference between rim and core (Table 2).

3.3 | Carbon isotope composition of Mendon cherts

Bulk rock samples have organic C concentrations between 0.03 and 1.5 wt.% and $\delta^{13}C$ values between −32.1 and −26.5‰ (Table 3 and Figure 4) in the range previously determined for Mendon formation (Hofmann & Bolhar, 2007; Walsh & Lowe, 1999). Data from Noel master's thesis (Noel, 2009) are also reported and give similar results (Figure 4). Samples with the highest organic carbon contents show the lowest $\delta^{13}C$ values, as frequently observed in

Precambrian sediments (Guy et al., 2012; Luo et al., 2014; Peng et al., 2019).

3.4 | Iron and sulfur isotope compositions of pyrite

In the 12 samples investigated, a total of 109 pyrites were analyzed for both S and Fe isotope compositions, with multiple analyses of the largest pyrite crystals (Table 4). Pyrites in the Mendon Formation show large isotope variability in δ^{56}Fe, δ^{34}S, and Δ^{33}S, which is not related to the stratigraphic position within the core (Figure 5). δ^{34}S and Δ^{33}S values range from −2.66 to +6.22‰ and −0.39 to +4.25‰, respectively (Figures 5 and 6a), consistent with previous reports on the same formation (Galić et al., 2016; Montinaro et al., 2015; Roerdink, Mason, Whitehouse, & Reimer, 2013). The δ^{56}Fe values vary from −4.02 to +2.54‰, covering almost the total terrestrial range reported so far (Dauphas, John, & Rouxel, 2017). Some samples show large δ^{56}Fe variations up to 6‰ (Sample 160.12) with small S isotopic variability, while others have large range of δ^{34}S values (samples 95.41 and 147.38) with smaller range of variations in δ^{56}Fe (Figures 5 and 6). There is no correlation between δ^{34}S and δ^{56}Fe values (Figure 6b).

In order to better illustrate the isotopic variability of each sample, a probability density distribution was calculated for each sample. Each measurement (δ^{56}Fe, σ) is replaced by a Gaussian curve $f_{\delta^{56}\mathrm{Fe},\sigma}$ such as:

$$f_{\delta^{56}\mathrm{Fe},\sigma}(x) = \frac{1}{\sigma \times \sqrt{2\pi}} \times \exp\left[\frac{-\left(-x-\delta^{56}\mathrm{Fe}\right)^2}{2\sigma^2}\right] \quad (1)$$

The integral of $f_{\delta^{56}\mathrm{Fe},\sigma}$ between x_1 and x_2 gives the probability that the true δ^{56}Fe of the sample is between x_1 and x_2. The probability density function $F(x)$ describing δ^{56}Fe variations in a sample is defined for N measurements as the sum of individual $f_{\delta^{56}\mathrm{Fe},\sigma}$ divided by N:

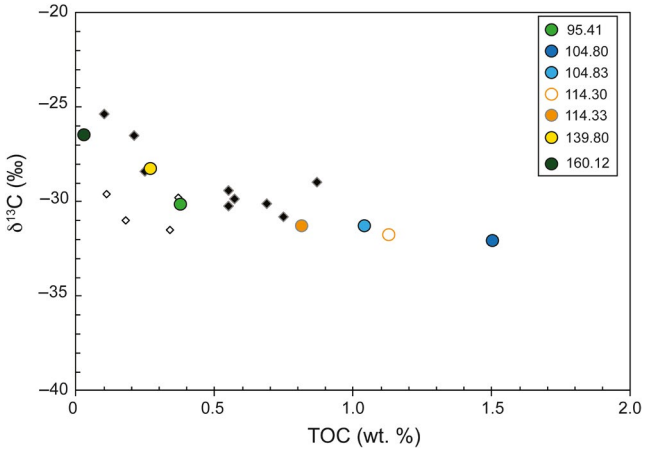

FIGURE 4 TOC and δ^{13}C values of the different pyrite groups. Data from the same formation published by Hofmann & Bolhar, 2007 and master's thesis from Vincent Noel are also reported in white and black, respectively

$$F(x) = \sum_{j=1}^{j=N} \frac{f_{\delta^{56}\mathrm{Fe}_j,\sigma_j}(x)}{N} \quad (2)$$

with the probability $P(x) = \int_{-\infty}^{+\infty} F(x) \times dx = 1$.

For example, if $\int_{-2.0}^{-2.5} F(x) \times dx = 0.4$, then the probability for a nanopyrite showing δ^{56}Fe values lying between −2.5‰ and −2.0‰ is 40%.

4 | DISCUSSION

Pyrites from the Mendon cherts display a large range of isotopic compositions both in Fe and S, which is not correlated with the size or shape of pyrites. The sample stratigraphic position does not correlate with Fe and/or S isotope compositions (Figure 5). However, Δ^{33}S correlates with crystallinity order, with values around 0‰ for well-crystallized pyrites and values higher than 2‰ for polycrystal-hosting pyrites (Figure 7). Three different pyrite populations can be distinguished based on their δ^{56}Fe and Δ^{33}S values (Figure 7a). These are Group A with mean δ^{56}Fe of −1.76 ± 0.6‰ (1σ) and Δ^{33}S of −0.05 ± 0.3‰ (1σ; samples 137.84, 104.8, and 104.83 and few pyrites from 160.12), Group B with δ^{56}Fe of +1.05 ± 0.4‰ (1σ) and Δ^{33}S of +0.67 ± 0.5‰ (1σ; samples 94.92, 95.41, 133.55, 139.80, 147.38, and 160.12), and Group C with δ^{56}Fe averaging +1.01 ± 0.9‰ and Δ^{33}S of +3.5 ± 0.6‰ (1σ; samples 114.3 and 114.33). It is worth noting that some samples (e.g., 160.12) contain pyrite grains that belong to two different groups. The following discussion will focus on constraining the origin of the large isotopic variability in both Fe and S compositions by assessing first, the influence of fluid circulation and hydrothermal overprint, second, the different pyrite group origin and pyrite formation pathways, and lastly, the potential microbial origin of these isotope compositions.

4.1 | Role of hydrothermal processes on Fe and S isotopic compositions

All pyrites from Mendon cherts contain mineral inclusions of either quartz or carbonate and can thus be considered as a late phase related to diagenesis. Post-diagenetic and hydrothermal processes should lead to pyrite recrystallization with variable trace element enrichments such as Co, Ni, and Pb, depending on the fluid chemistry (Large, Maslennikov, Robert, Danyushevsky, & Chang, 2007). In Mendon samples, trace element concentrations of the different pyrite groups are similar (Table 2) and display no detectable enrichments in Co, Mn, Zn, and Pb above the detection limits of EPMA technique (>100 ppm, see section 2.2.2). Chemical profiles obtained across large pyrite grains show homogenous and low concentration in terms of trace element distribution patterns (Table 2). The absence of trace element enrichment argues against a late stage of pyrite overgrowth, which contrasts with SEM and TEM observations. Among the few cases where Co was detected, Co/Ni ratio was always below 0.6, supporting a sedimentary rather than a metamorphic origin for these pyrites (Gregory et al., 2015). It is worth emphasizing that Group B

TABLE 4 S and Fe isotope composition of pyrite from the Mendon cherts

	Sample	d56Fe	err	*d34S*	err	*D33S*	err
Group A							
104.80-2pt70	104-80	−1.99	0.32	5.56	0.16	−0.02	0.07
104.80-2pt71	108-80	−1.51	0.32	2.56	0.18	1.48	0.07
104.80-2pt72	104-80	−3.30	0.32	6.06	0.18	−0.39	0.07
104.80-2pt73	104-80	−4.02	0.32	5.71	0.16	−0.21	0.07
104.80-2pt75	108-80	−2.20	0.32	6.21	0.16	−0.16	0.07
104.80-2pt76	104-80	−2.05	0.32	6.22	0.16	−0.20	0.07
104.80-2pt78	108-80	−1.84	0.32	5.39	0.17	−0.06	0.07
104.80-2pt79	104-80	−1.56	0.32	2.35	0.16	−0.30	0.07
104.80-2pt80	104-80	−1.05	0.32	−0.72	0.17	−0.11	0.07
104.80-2pt81	108-80	−1.88	0.32	2.01	0.16	−0.07	0.07
104.80-2pt82	108-80	−0.89	0.32	4.77	0.16	−0.20	0.07
104.80-2pt83	104-80	−0.51	0.32	5.93	0.17	−0.10	0.07
104.80-2pt84	108-80	−1.95	0.32	5.87	0.17	−0.05	0.07
104.80-2pt85	104-80	−1.85	0.32	5.37	0.17	−0.11	0.07
104.80-2pt87	104-80	−1.54	0.32	5.15	0.17	−0.19	0.07
104.80-2pt88	108-80	−2.00	0.32	6.06	0.16	−0.25	0.07
104.80-2pt89	108-80	−1.93	0.32	1.79	0.16	−0.11	0.07
104.80-2pt91	104-80	−1.25	0.32	−0.11	0.16	−0.02	0.07
104.80-2pt92	108-80	−1.39	0.32	0.09	0.16	−0.13	0.07
104.80-2pt93	104-80	−2.05	0.42	4.63	0.16	−0.29	0.07
104.80-2pt94	104-80	−0.54	0.32	6.00	0.17	−0.24	0.07
104.80-2pt95	108-80	−1.23	0.32	5.71	0.17	0.10	0.07
104.83-1pt99	104-83	−1.54	0.32	5.11	0.17	−0.20	0.07
104.83-1pt100	104-83	−1.48	0.32	2.47	0.16	−0.29	0.07
104.83-1pt101	104-83	−1.55	0.32	0.30	0.17	0.00	0.07
104.83-1pt102	104-83	−1.66	0.32	4.94	0.16	−0.13	0.07
104.83-1pt103	104-83	−1.95	0.32	5.92	0.17	−0.23	0.07
104.83-1pt104	104-83	−1.76	0.32	5.44	0.17	−0.15	0.07
104.83-1pt105	104-83	−1.87	0.32	4.04	0.17	−0.11	0.07
104.83-1pt106	104-83	−1.38	0.32	2.54	0.17	−0.16	0.07
104.83-1pt107	104-83	−1.75	0.33	3.42	0.17	−0.27	0.07
104.83-1pt109	104-83	0.90	0.32	3.32	0.17	−0.14	0.07
104.83-4pt111	104-83	−1.95	0.32	4.87	0.17	−0.33	0.07
104.83-4pt112	104-83	−1.84	0.32	1.04	0.18	−0.09	0.07
104.83-4pt113	104-83	−1.80	0.32	0.47	0.18	0.02	0.07
104.83-4pt114	104-83	−1.47	0.32	2.29	0.17	−0.26	0.07
104.83-4pt115	104-83	−1.76	0.32	3.39	0.17	−0.28	0.07
104.83-4pt116	104-83	−1.84	0.32	4.56	0.17	−0.25	0.07
104.83-4pt117	104-83	−1.77	0.32	4.38	0.17	−0.02	0.07
104.83-4pt119	104-83	−1.92	0.32	4.98	0.17	−0.26	0.07
104.83-4pt120	104-83	−2.17	0.32	5.83	0.17	−0.34	0.07
104.83-4pt122	104-83	−2.08	0.32	0.05	0.17	−0.05	0.07
104.83-4pt123	104-83	−1.81	0.32	3.58	0.17	−0.08	0.07
104.83-4pt125	104-83	−1.96	0.32	1.28	0.17	0.06	0.07

(Continues)

TABLE 4 (Continued)

	Sample	d56Fe	err	*d34S*	err	*D33S*	err
104.83-4pt126	104-83	−2.10	0.32	4.55	0.17	−0.28	0.07
104.83-4pt127	104-83	−2.00	0.32	1.45	0.18	−0.16	0.07
104.83-4pt128	104-83	−1.80	0.32	1.56	0.17	1.68	0.07
104.83-4pt129	104-83	−1.52	0.32	5.03	0.17	−0.21	0.07
104.83-5pt130	104-83	−2.71	0.32	3.96	0.18	−0.03	0.07
104.83-5pt131	104-83	−2.38	0.32	5.25	0.18	−0.27	0.07
104.83-5pt132	104-83	−2.21	0.32	3.31	0.18	−0.28	0.07
104.83-5pt134	104-83	−2.75	0.32	5.52	0.17	−0.03	0.07
104.83-5pt135	104-83	−1.89	0.32	5.56	0.16	−0.04	0.07
104.83-5pt136	104-83	−1.95	0.32	3.36	0.17	−0.17	0.07
104.83-5pt137	104-83	−1.59	0.32	0.39	0.18	−0.13	0.07
137.84b-1-pt30	137-84	−1.60	0.31	4.47	0.16	0.34	0.07
137.84b-1-pt31	137-84	−1.81	0.32	4.76	0.16	0.22	0.07
137.84b-1-pt32	137-84	−1.51	0.32	4.57	0.16	0.35	0.07
137.84b-1-pt33	137-84	−1.67	0.32	4.91	0.16	0.43	0.07
137.84b-1-pt34	137-84	−1.68	0.32	4.65	0.16	0.32	0.07
137.84b-1-pt35	137-84	−1.39	0.31	4.62	0.16	0.32	0.07
137.84b-1-pt36	137-84	−1.35	0.31	4.72	0.16	0.13	0.07
Group C							
114-3-pt@03	114-30	0.89	0.26	−0.89	0.24	2.69	0.13
114-3-pt@07	114-30	0.84	0.25	0.43	0.58	3.16	0.07
114-3-pt@09	114-30	1.17	0.26	1.64	0.25	4.11	0.13
114-3-pt@1	114-30	2.24	0.26	0.64	0.58	3.37	0.07
114-3-pt@11	114-30	2.51	0.26	−0.78	0.25	3.82	0.13
114-3-pt@12	114-30	2.54	0.25	2.94	0.30	3.93	0.09
114-3-pt@13	114-30	1.45	0.27	2.87	0.30	4.25	0.08
b114-30@1	114-30	0.53	0.35	0.43	0.58	3.16	0.07
b114-30@02	114-30	1.49	0.36	−2.66	0.58	3.20	0.07
b114-30@03	114-30	1.57	0.36	0.44	0.58	2.79	0.07
b114-30@04	114-30	2.40	0.35	−0.99	0.58	3.35	0.07
b114-30@05	114-30	1.83	0.36	0.64	0.58	3.37	0.07
b114-30@07	114-30	0.65	0.35	0.53	0.58	3.17	0.07
114-33-2-10	114-33	0.39	0.32	2.14	0.63	4.13	0.53
114-33-2-3	114-33	0.41	0.32	2.23	0.63	4.05	0.53
114-33-2-4	114-33	−0.58	0.32	2.26	0.63	3.90	0.53
114-33-2-8	114-33	−0.86	0.32	1.79	0.65	3.64	0.60
114-33-2-9	114-33	−0.25	0.32	1.56	0.63	4.05	0.53
130-80-pt@1	139-80	2.32	0.24	3.94	0.23	2.32	0.05
E2-139-80@1	139-80	0.33	0.35	2.79	0.22	2.32	0.05
E2-139-80@2	139-80	0.40	0.36	n.a	n.a	n.a	n.a
E2-139-80@3	139-80	0.87	0.35	4.50	0.20	3.71	0.05
E2-139-80@4	139-80	0.66	0.35	2.79	0.22	2.32	0.05
E2-139-80@5	139-80	1.05	0.36	1.05	0.22	2.93	0.05
E2-139-80@6	139-80	0.30	0.35	n.a	n.a	n.a	n.a

(Continues)

TABLE 4 (Continued)

	Sample	d56Fe	err	*d34S*	err	*D33S*	err
Group B							
94-92@4	94-92	1.27	0.26	3.01	0.23	0.29	0.05
94-92@6	94-92	1.20	0.26	3.99	0.24	0.12	0.05
94-92@7	94-92	1.63	0.25	2.78	0.23	1.08	0.05
94-92@8	94-92	0.74	0.25	4.76	0.22	0.29	0.05
95-41@07	95-41	0.99	0.25	2.62	0.23	0.13	0.05
95-41@08	95-41	2.21	0.26	1.31	0.19	0.41	0.05
95-41@09	95-41	0.61	0.25	4.16	0.23	0.20	0.05
95-41@10	95-41	0.80	0.25	3.16	0.23	0.78	0.05
95-41@11	95-41	0.95	0.25	2.86	0.22	1.40	0.05
95-41@12	95-41	1.03	0.25	3.25	0.23	0.32	0.05
95-41@19	95-41	0.44	0.25	3.37	0.21	0.13	0.05
95-41@20	95-41	1.04	0.26	4.19	0.22	0.03	0.05
95-41@21	95-41	1.08	0.25	4.77	0.22	0.14	0.05
95-41@22	95-41	1.02	0.25	3.41	0.23	0.33	0.05
95-41@23	95-41	1.17	0.25	−2.31	0.25	1.13	0.05
E2-95-41@1	95-41	0.64	0.36	2.93	0.23	0.19	0.03
E2-95-41@03	95-41	0.12	0.35	1.92	0.23	0.77	0.03
E2-95-41@04	95-41	0.66	0.36	1.63	0.22	1.40	0.03
E2-95-41@06	95-41	0.59	0.36	2.01	0.23	0.31	0.03
135-55-pt@08	135-55	1.30	0.25	2.55	0.34	0.59	0.06
135-55-pt@09	135-55	1.37	0.26	2.68	0.33	0.83	0.06
135-55-pt@12	135-55	0.96	0.25	2.92	0.33	0.56	0.06
135-55-pt@13	135-55	1.06	0.25	3.12	0.33	0.50	0.06
135-55-pt@14	135-55	0.97	0.25	3.31	0.33	0.76	0.06
135-55-pt@15	135-55	1.63	0.25	1.77	0.33	−0.01	0.06
135-55-pt@16	135-55	0.95	0.25	3.37	0.33	0.51	0.06
135-55-pt@17	135-55	0.78	0.25	1.06	0.32	0.28	0.06
135-55-pt@21	135-55	0.81	0.25	3.41	0.33	0.59	0.06
135-55-pt@22	135-55	1.01	0.25	3.48	0.33	0.66	0.06
148-10-pt@02	148-10	1.49	0.25	−0.85	0.33	−0.12	0.06
148-10-pt@04	148-10	1.57	0.25	−2.49	0.31	0.36	0.06
148-10-pt@07	148-10	1.32	0.26	−0.98	0.33	2.28	0.06
148-10-pt@08	148-10	0.71	0.25	4.30	0.33	−0.20	0.06
148-10-pt@12	148-10	1.18	0.25	1.43	0.33	−0.07	0.06
148-10-pt@13	148-10	1.07	0.25	4.42	0.33	−0.20	0.06
148-10-pt@15	148-10	1.79	0.25	*3.95*	0.33	−0.22	0.03
C147-38@01	148-10	0.69	0.35	−1.88	0.33	−0.15	0.03
C147-38@06	148-10	1.11	0.35	3.17	0.33	−0.02	0.03
C147-38@07	148-10	0.83	0.35	*4.50*	0.33	−0.07	0.03
C147-38@10	148-10	1.15	0.35	−1.26	0.33	0.06	0.33
160-12-2@02	160-12	0.81	0.25	1.29	0.24	0.12	0.05
160-12-2@03	160-12	0.27	0.25	1.41	0.24	0.04	0.05
160-12-2@05	160-12	−2.39	0.24	1.19	0.24	0.12	0.05
160-12-2@06	160-12	−3.30	0.25	1.94	0.24	0.44	0.05

(Continues)

TABLE 4 (Continued)

	Sample	d56Fe	err	*d34S*	err	*D33S*	err
160-12-2@08	160-12	−2.15	0.26	1.21	0.24	−0.13	0.05
160-12-2@1	160-12	1.47	0.25	0.00	0.25	−0.25	0.05
E2-160-12@1	160-12	0.65	0.37	−0.03	0.24	−0.13	0.03
E2-160-12@2	160-12	0.73	0.37	0.06	0.24	0.11	0.03
E2-160-12@3	160-12	0.79	0.35	0.93	0.23	0.63	0.03

pyrite can contain up to 1,700 ppm Ni, but that this enrichment is homogenously distributed throughout the pyrite grains. Group C pyrites show the lowest trace element concentrations, with values typically under the detection limits. Therefore even if the Mendon cherts have experienced hydrothermal fluid circulations (Busigny et al., 2017), these late events have not significantly modified the original pyrite trace element concentrations.

The effect of fluid circulation on iron isotope compositions of Mendon pyrite can also be evaluated. For an equilibration temperature of ~350°C (Tice et al., 2004), pyrite precipitated from a Fe(II)-bearing fluid should have been in, or near to, isotopic equilibrium. Assuming a hydrothermal fluid with δ^{56}Fe values between −0.5 and 0‰ (e.g., Severmann et al., 2004; Rouxel, Sholkovitz, Charette, & Edwards, 2008; Johnson et al., 2008) and a fractionation of ~1‰ between pyrite and Fe(II) dissolved in the fluid (Polyakov et al., 2019; Syverson, Borrok, & Seyfried Jr, 2013), the δ^{56}Fe values of pyrite precipitated from this fluid should range between +0.5 and +1‰. These values are compatible with the pyrites from Groups B and C (Figure 6), but not with those of Group A. Additionally, pyrite formed under hydrothermal conditions should be well-crystallized, which is not the case of the Group C pyrites. We therefore conclude that a secondary hydrothermal alteration process could account for the Fe isotope compositions of Group B pyrites but not for those of Groups A and C pyrites. We note that comparable Fe isotope profiles obtained in Groups B and C pyrites (Figure 8) supports a related formation process.

Similarly, the influence of fluid circulations on sulfur isotope compositions can be examined. Sulfur in late fluid circulations can have a juvenile origin characterized by a δ^{34}S of 0‰ and no S-MIF signatures with Δ^{33}S = 0‰ (Labidi, Cartigny, & Jackson, 2015). Sulfur isotope profiles through large pyrites (more than 10 isotopic profiles measured in different pyrite grains) from each group highlight the presence of positive Δ^{33}S values in all the pyrite groups (Figure 8). Group C pyrite displays homogenous distributed Δ^{33}S throughout the grains, while Group B and Group A show a zoning pattern with non-zero Δ^{33}S cores and Δ^{33}S ~0‰ rims (Figure 8). Pyrites from sample 147.38 show large isotopic variations in δ^{56}Fe (~2‰) and δ^{34}S values (~6‰), with high δ^{56}Fe and low δ^{34}S cores, and low δ^{56}Fe and high δ^{34}S rims. These isotopic profiles are consistent with a late stage of pyrite overgrowth associated with the infiltration of a fluid phase of different S composition as already suggested by Marin-Carbonne et al. (2014). Note, however, that some Group C pyrites (sample 114.30), displaying the same range of ~2‰ δ^{56}Fe variation from core to rim, show homogeneous Δ^{33}S and δ^{34}S profiles, thus arguing for different fluid sources during rim crystallization (Figure 8). The presence of S-MIF in each pyrite group indicates that the sulfur source is of atmospheric origin. The absence of a Δ^{33}S anomaly in the rim of pyrite grains from Groups B and C indicates that a mantle-derived fluid source (Δ^{33}S = 0‰) contributed to some of the pyrite overgrowth. This observation contrasts with the absence of core–rim variations recorded from trace element concentrations and Fe isotope compositions, which supports the conclusions

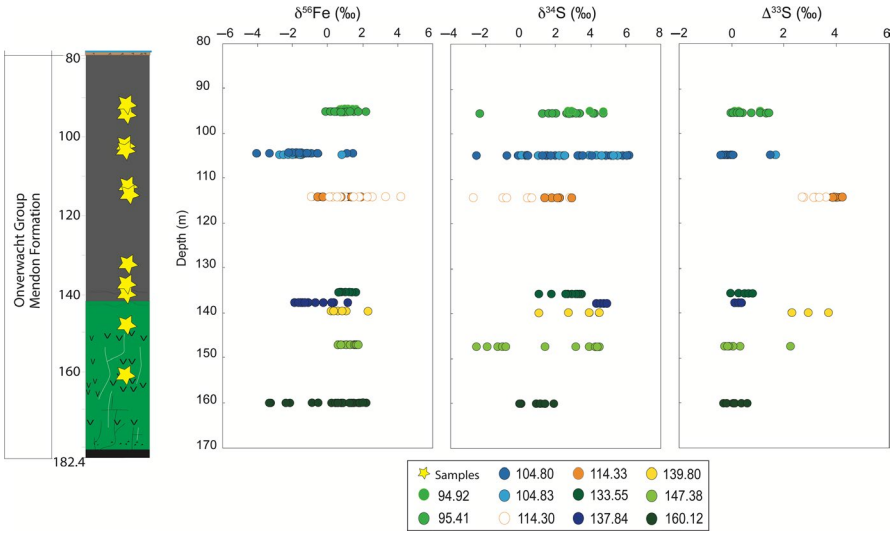

FIGURE 5 δ^{56}Fe, δ^{34}S, and Δ^{33}S isotope profiles along the BBDP2 core. There is no relationship between Fe and S isotope compositions and the sample depth. Some samples display homogeneous isotope composition, while others (e.g., 104.80 or 114.30) show large isotopic variability. Some single grains show large internal variability, up to 4‰ for δ^{34}S. Most samples have Δ^{33}S values close to 0‰, while only 5 samples have Δ^{33}S values > 0‰ (94.92, 104.80, 114.30, 147.38, and 160.12)

already reached by Marin-Carbonne et al. (2014) on pyrite and Li, Konhauser, Kappler, and Hao (2013) on magnetite that there can be a decoupling between different geochemical tracers during mineral recrystallization.

Altogether, the trace element concentrations, δ^{56}Fe and Δ^{33}S isotope variabilities at a micrometer scale, pinpoint a sedimentary origin of these pyrites or their precursors.

4.2 | Pyrite origin and formation pathways

Pyrite formation is a complex two-step process involving slow pyrite nucleation and fast crystal growth (Rickard, 2012). Pyrite can be formed from various precursors either iron monosulfide like mackinawite (FeS) or polysulfide like greigite (Fe_3S_4) (Rickard, 2012). The precursor minerals always dissolve to form aqueous FeS complexes, which then react with H_2S or polysulfides to form pyrite (Rickard, 2012).

The presence of positive Δ^{33}S values in all pyrite groups suggests that pyrite precipitated from elemental sulfur. Elemental sulfur with positive Δ^{33}S values was likely produced via photochemical reactions in oxygen-free Archean atmosphere (e.g., Farquhar et al., 2000) and was preferentially delivered to the sediments rather than processed in the water column, as insoluble and unreactive particles (Rickard, 2012). However, pyrite cannot form directly from particulate elemental S (Rickard & Luther, 2007). Before reacting with a dissolved pyrite precursor, an intermediate step to break S_8 rings is required (Rickard, 2012). In sedimentary pore waters, S_8 rings were possibly gradually opened and sulfur chains and compounds were biologically converted to H_2S, for example, through disproportionation. The pyrites from Mendon Formation likely formed by late recrystallization of pyrite precursors. As discussed above, this recrystallization process modified the S isotope composition but not the Fe isotope composition. As the formation of pyrite after mackinawite only requires sulfur addition, the lack of Fe isotope composition changes suggests that mackinawite rather than greigite was the precursor phase.

How confidently pyrite δ^{56}Fe values reflect the isotopic composition of the parent Fe(II) remains subject of debates (Beard et al., 1999; Busigny et al., 2014; Frierdich, Nebel, Beard, & Johnson, 2019; Guilbaud, Butler, & Ellam, 2011; Mansor & Fantle, 2019; Rolison et al., 2018). For instance, as shown by Guilbaud et al. (2011) and Rolison et al. (2018), the transformation of mackinawite to pyrite can induce an Fe isotope fractionation of ~−3‰ without involvement of any redox reaction. Such a kinetic fractionation process could therefore account, in principle, for most of the isotopic heterogeneities recorded in the studied samples. However, a kinetic fractionation process also implies that the resulting pyrite δ^{56}Fe values should display a Rayleigh distribution with a maximum centered on the δ^{56}Fe value of the Fe(II) source, which is not observed. Instead, our data show a bimodal distribution with two major peaks around −1.8 and +1.0‰ (Figure 7b). In addition, as reported in modern environments like the Black Sea, a kinetic fractionation process requires transient ferruginous and euxinic conditions (Rolison et al., 2018). This is at odd with our current knowledge of ocean chemistry at 3.2 Gyr, where ferruginous conditions were likely persistent (Lyons, Reinhard, & Planavsky, 2014).

A recent study of Mansor and Fantle (2019) proposed that pyrite δ^{56}Fe value can be controlled by its precipitation rate. Negative δ^{56}Fe values would reflect the expression of kinetic isotopic effect (KIE), while positive δ^{56}Fe values would correspond to equilibrium isotopic effect (EIE). Taken at face value, this would imply that the bimodal distribution of δ^{56}Fe values reflects different rates of pyrite precipitation controlled either by kinetic or equilibrium fractionation. If correct, some correlation between pyrite morphology, size, and iron isotope composition would be expected. As suggested by Mansor and Fantle (2019), precipitation rate will be different for large cubic pyrite grain than for small pyrite aggregates. However, large pyrite grains show either negative (sample 104.83) or positive δ^{56}Fe values (sample 114.30), and there is no apparent correlation between the size and Fe isotope composition of the pyrites. For example, sample 133.55 displays a large range of pyrite sizes, from 10 μm to 1 mm, while the Fe isotope composition of these pyrites is quite homogeneous (mean δ^{56}Fe of +1.12 ± 0.28‰ for 24 pyrite grains with variable size).

In addition, the marked change from positive to negative δ^{56}Fe values across a single pyrite grain from Group B and C (Figure 8)

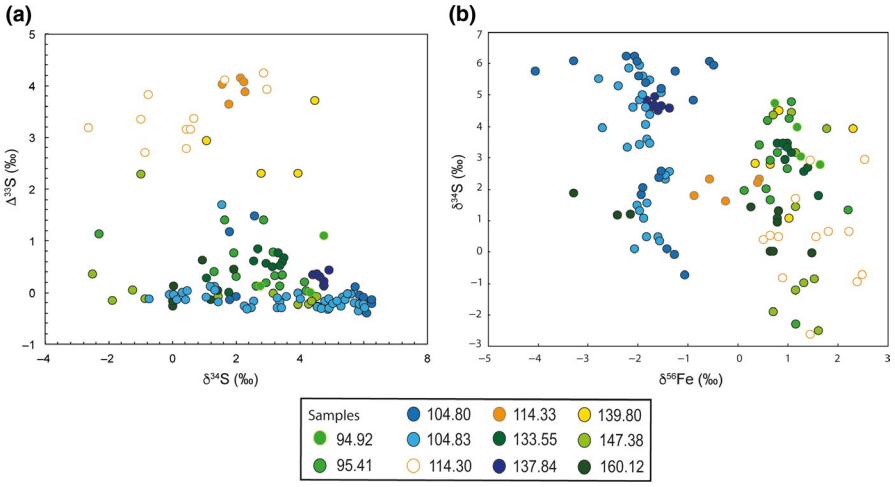

FIGURE 6 (a) δ^{34}S and Δ^{33}S compositions and (b) δ^{34}S and δ^{56}Fe values of the Mendon pyrites. Error bars are comprised in the dot

would imply that the rate of pyrite precipitation changed drastically during pyrite formation. The model of Mansor and Fantle (2019) predicts that pyrite nucleation and early stages of crystal growth should be associated with high rate of precipitation (*i.e.*, kinetically dominated and low δ^{56}Fe values), while later stages should evolve toward lower rates of precipitation (closer to equilibrium, with higher δ^{56}Fe values). This prediction is opposite to our Fe isotope profiles in Groups B and C pyrite and is not clearly observed in Group A (Figure 8). This prediction is also not consistent with textural observations, as all pyrite cores from the different groups are polycrystalline and should therefore reflect a same precipitation rate, but group A displays negative δ^{56}Fe values, while Group B and C pyrites display positive δ^{56}Fe values. Additionally, if Fe isotope compositions were influenced by the rate of pyrite precipitation and kinetic effect, this should have also influenced the S isotopic compositions as suggested by modeling studies (Hegyi & Halevy, 2019; Johnston, Hemingway, Gill, & Halevy, 2019; Raiswell, Whaler, Dean, Coleman, & Briggs, 1993). Pyrite rims and cores should display different δ^{34}S values, which has been recorded in only one sample from Group B (147.38) but not in Groups A and C pyrites and other samples from Group B (95.41, Figure 8). With the exception of one sample from Group B, there is no marked variation of δ^{34}S values between pyrite cores and rims.

The large range of Fe and S isotope compositions recorded in Mendon pyrites can be explained by various pyrite precursors. In this case, the bimodal distribution of δ^{56}Fe values (Figure 7) would reflect two different pyrite precursors, one with negative δ^{56}Fe and positive Δ^{33}S values and one with positive δ^{56}Fe and Δ^{33}S values. The negative δ^{56}Fe origin of the pyrite precursor may be explained by a kinetic process (see below), while the positive δ^{56}Fe values of the precursor would have originated from iron oxides reduction either abiotically or biologically induced by DIR (Yoshiya et al., 2015). How concomitant these pyrite precursors would have been formed is still unknown. In such a scenario, different pyrite groups would reflect different pyrite generations. The similarity in microscale mineralogy and trace element contents is difficult to reconcile with different pyrite precursors but most likely reflects diagenetic processes. Accordingly, we suggest the Mendon pyrites were most likely formed through the transformation of the precursor mackinawite, which would be best represented by the fine-grained and polycrystalline nature (Rickard, 2012) of some pyrite cores (Group C).

4.3 | Biosignature of dissimilatory iron reduction recorded in pyrites

Groups A and B display similar Δ^{33}S but distinct δ^{56}Fe values (Figures 7 and 8). The negative δ^{56}Fe values of Group A are comparable to most Archean sedimentary pyrites (Planavsky et al., 2012), which are usually interpreted as reflecting DIR (Johnson et al., 2008), kinetic isotope fractionation associated with pyrite precipitation (Guilbaud et al., 2011; Rolison et al., 2018), and/or a distillation effect of oceanic dissolved Fe(II) due to Fe oxide precipitation (Rouxel, Bekker, & Edwards, 2005). In contrast, high δ^{56}Fe values of Group B pyrites are more occasional for Archean pyrites (Johnson et al., 2008; Rouxel et al., 2005), but rather typical of iron oxides formed from partial oxidation of a large Fe(II) reservoir (Planavsky et al., 2012; Rouxel et al., 2005). Interestingly, the samples hosting Group B pyrites do not contain iron oxide contrary to samples from Group A (Figure 9). This suggests that Group B pyrites with positive δ^{56}Fe values were derived from total reduction in former iron oxides, thus preserving their original Fe isotope compositions (near + 1‰). In contrast, Group A pyrites with negative δ^{56}Fe values could have formed from dissolved Fe(II) released by partial reduction in iron oxides and, therefore, could record the composition of dissolved Fe(II). Although—as discussed above—a kinetic isotope fractionation associated with pyrite precipitation cannot be ruled out, the absence (in Group B) or presence (in Group A) of residual Fe oxides is more supportive of a prominent effect of Fe reduction. Following this scenario, the difference in Fe isotope composition between Group A and B pyrites could reflect the fractionation associated with iron oxide reduction, which can be estimated at about −2.8‰ (Figure 7). This Fe isotope fractionation is remarkably similar to the one determined experimentally

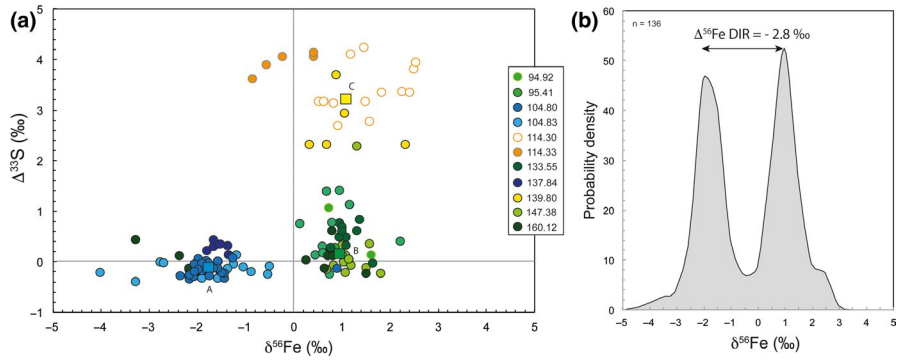

FIGURE 7 (a) δ^{56}Fe and Δ^{33}S values of the Mendon pyrites display three different groups (A in blue, B in green, and C in orange/yellow). There is no correlation with the stratigraphic location (Figure 5). Error bars are comprised within the dots. The mean value of each group is reported as a square with the respective color of each pyrite group. (b) Probability density function of δ^{56}Fe values for all pyrites showing bimodal distribution with a difference of ~2.8‰ interpreted as reflecting isotope fractionation associated with microbial Fe respiration

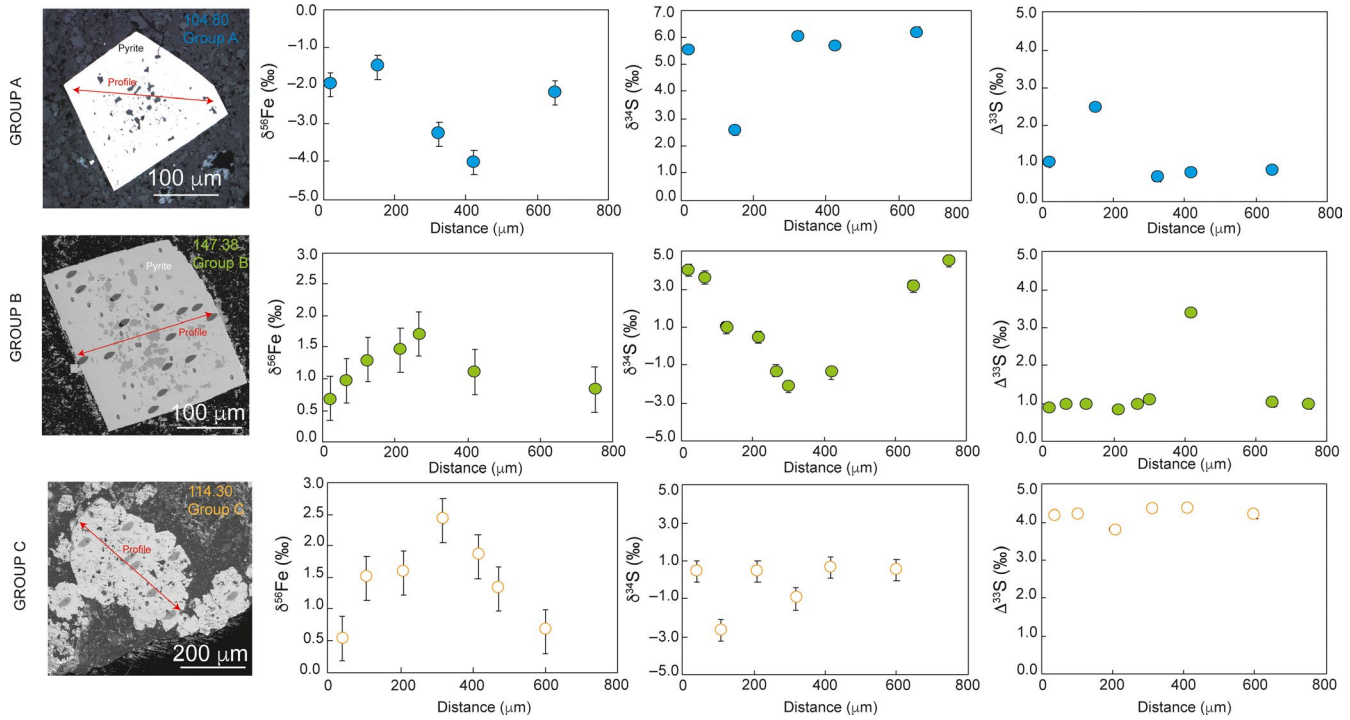

FIGURE 8 SEM pictures, $\delta^{56}Fe$, $\delta^{34}S$, $\Delta^{33}S$ isotopic profiles in individual pyrite grain from each pyrite groups. Errors bars are comprised in the dot

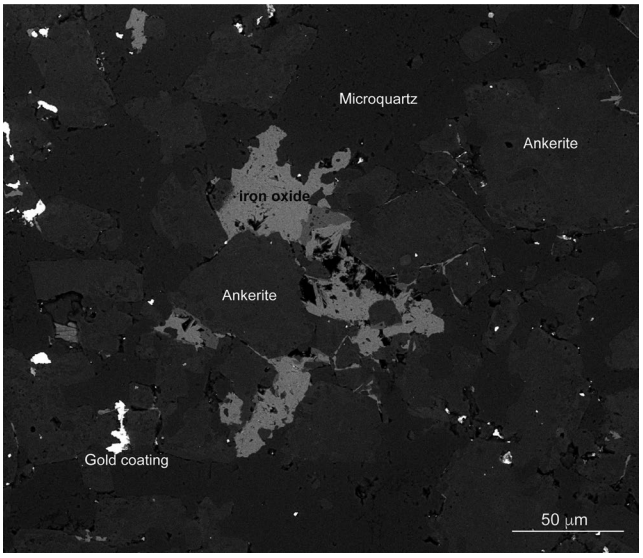

FIGURE 9 SEM picture of iron oxides present in Group A pyrites. These iron oxides, potentially hematite, are embedded in the microquartz matrix and often associated with iron carbonates

for microbial DIR (Crosby et al., 2007; Johnson & Beard, 2005), but also with abiotic reduction at low temperature (e.g., Frierdich et al., 2019). However, this isotopic fractionation is not compatible with abiotic reduction related to burial and/or interaction with metamorphic fluids. A reduction associated with hydrothermal overprints such as those experienced by Mendon cherts is unlikely because re-equilibration at about 350°C should have reduced, not increased the Fe isotope fractionation (Dauphas et al., 2017). Therefore, the large and consistent Fe isotope fractionation can suggest that pyrite $\delta^{56}Fe$ values were inherited from early diagenetic microbial reduction and remained unaffected by subsequent hydrothermal alteration processes (Figure 10). Groups A and B pyrites were thus likely formed by a DIR process through partial and total Fe reduction, respectively. In contrast, the well-ordered crystallinity and $\Delta^{33}S$ values near 0‰ of Groups A and B pyrites point to sulfide recrystallization in the presence of S-rich mantle-derived fluids (Roerdink, Mason, Whitehouse, & Brouwer, 2016). The modification of the primary S isotope signature but preservation of the original Fe isotope imprint possibly arose from interaction of a precursor sulfide (e.g., most likely mackinawite) with a S-rich and Fe-poor hydrothermal fluid. Considering the mineralogy of the rocks and the diagenetic and metamorphic processes that are known to have affected the Barberton area, production and circulation of fluids enriched in sulfides must have been common, which could account for the precipitation of pyrite with no S-MIF signatures (Agangi, Hofmann, Eickmann, & Marin-Carbonne, 2019; Agangi, Hofmann, Eickmann, Marin-Carbonne, & Reddy, 2016).

Pyrites from Group C show more variable but mostly positive $\delta^{56}Fe$ values, averaging +1.01 ± 0.90‰ (1σ). The positive $\delta^{56}Fe$ values together with the absence of iron oxides in the samples suggest pyrite formation after total iron oxide reduction, like for Group B pyrites. Positive $\Delta^{33}S$ values of Group C pyrites argue for a volcanic source of sulfur equilibrated in an anoxic atmosphere (Johnston, 2011). Photochemical reactions of volcanic SO_2 in the Archean atmosphere are generally supposed to produce elemental sulfur (S^0) and sulfate (SO_4^{2-}) aerosols, with positive and negative $\Delta^{33}S$ values, respectively (Farquhar et al., 2000). Accordingly, our results suggest that pyrites from Group C derived, at least partly, from Archean atmospheric elemental sulfur. Pyrite $\delta^{34}S$ values are

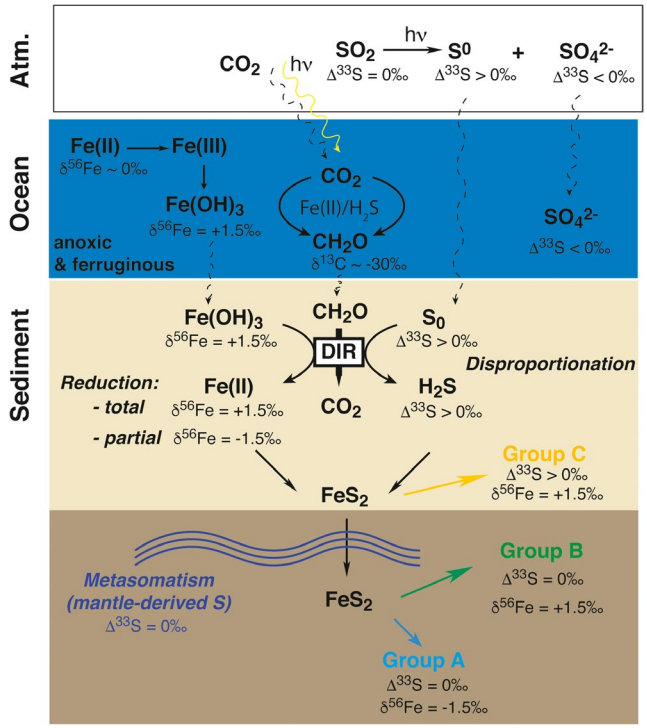

FIGURE 10 Biogeochemical model of the formation of pyrite from 3.28- to 3.26-Gyr-old cherts of the Mendon Formation. The model illustrates the environmental Fe and S compositions in the atmosphere, ocean, and sediment, as well as the various processes leading to the formation of pyrite. The three different groups of pyrites are shown in red. The DIR process took place in the sediment and was associated with sulfur disproportionation. A late metasomatic event modified S but not Fe isotope composition, implying interaction with an Fe-poor fluid

also consistent with microbial disproportionation of elemental sulfur (Figure 5, Johnston, 2011), as most disproportionating organisms produce fractionations between S^0 and H_2S smaller than 8‰ (Canfield, 2001). TEM analyses of pyrites from Group C reveal the persistence of polycrystalline particles (Figure 3b,c). These observations, as well as the finely laminated texture of the cherts hosting these pyrites, suggest a sedimentary origin, with better preservation than those of Groups A and B. Moreover, carbon isotope composition of organic matter hosted by Mendon black cherts ranges between −26 and −32.1‰ (Figure 4) and is consistent with a biological origin from phototrophic organisms (Schidlowski, Hayes, & Kaplan, 1983; Zerkle, House, & Brantley, 2005). Previous studies have highlighted the presence of micro-organisms during the deposition of cherts in the Onverwacht Group (Hofmann & Bolhar, 2007; Tice & Lowe, 2006; Walsh, 1992; Walsh & Lowe, 1999) and have excluded an hydrothermal origin of the organic matter (Hofmann & Bolhar, 2007; van Zuilen, Chaussidon, Rollion-Bard, & Marty, 2007). The presence of this fossil biomass supports the possibility for DIR activity, as this metabolic pathway involves iron-based oxidation of organic matter. It is worth noting that samples hosting Group A pyrites, which have experienced partial Fe reduction, have similar organic carbon contents and $\delta^{13}C$ values to those of Group C, which corresponds to total Fe oxide reduction (C_{org} ~0.82 to 1.51 wt.%, $\delta^{13}C$ ~−31.38 to −32.30‰; Figure 4). This indicates that organic matter availability was not the main limiting factor controlling partial versus total Fe reduction. Samples hosting pyrites from Group B have lower organic carbon content (C_{org} ~0.03 to 0.38 wt.%) and slightly less negative $\delta^{13}C$ values ($\delta^{13}C$ ~−26.57 to −30.18‰), showing that in this case the total reduction in iron has almost entirely consumed the organic matter (Figure 10).

5 | CONCLUSIONS

Taken together, Fe isotope data of Mendon pyrites from Groups A, B, and C show a bimodal distribution, demonstrating a large Fe isotope fractionation process (~2.8‰, Figure 7b) that can be ascribed to DIR. Anaerobic microbial respiration can simultaneously account for (a) the measured $\delta^{56}Fe$ systematic and variability and (b) the production of the reduced sulfur species necessary for pyrite formation. In addition, the light $\delta^{13}C$ values recorded in associated organic matter likely reflect the residual biomass derived from phototrophic organisms and consumed through joint Fe and S metabolisms during diagenesis. In contrast, the mineral assemblages and associated isotopic signals are difficult to explain by the abiotic processes discussed above. Our data extend reliable evidence of DIR metabolism back more than ~500 Myr than previously accepted (2.7 and 2.5 Gyr, Archer & Vance, 2006; Craddock & Dauphas, 2011). This supports indirect evidence from phylogenetic analyses and microbial culture studies for DIR origin in the early Archean, and therefore a close relation to the last universal common ancestor (Lonergan et al., 1996; Lovley, 2002; Vargas, Kashefi, Blunt-Harris, & Lovley, 1998). Interestingly, some DIR bacteria are known to reduce elemental sulfur enzymatically through disproportionation reactions producing both sulfide and sulfate (Flynn, O'Loughlin, Mishra, DiChristina, & Kemner, 2014; Thamdrup, Finster, Hansen, & Bak, 1993). This metabolic process could explain the formation of sulfide even in a very low sulfate environment (Berg et al., 2019; Crowe et al., 2014), but also the occurrence of pyrite displaying S isotopic compositions inherited from elemental sulfur in the Archean geological record. The presence of DIR in the Mendon Formation predating the deposition of banded iron formations (BIF) in the overlying Fig Tree Formation is also significant, as this metabolism is considered to be essential in the formation of BIF (Konhauser et al., 2017; Li et al., 2013). Indeed, DIR could explain the low content of organic carbon, the negative carbon isotope values of iron carbonates (Craddock & Dauphas, 2011), as well as the presence of other Fe(II)-bearing minerals (Li et al., 2013) in BIF. Combined with the positive $\Delta^{33}S$ values recorded in Mendon pyrites, this may indicate the antiquity of coupled microbial iron and sulfur metabolic pathways.

ACKNOWLEDGMENTS

Nordine Bouden and Etienne Deloule (CRPG-CNRS, Nancy) are thanked for their help during the IMS 1280 analysis sessions and David Troadec (IEMN, University of Lille) for preparing the FIB

sections. We thank Jean-Michel Guigner for his expert support of the TEM at IMPMC. The members of the GPI are thanked for fruitful discussions.

ORCID

Johanna Marin-Carbonne https://orcid.org/0000-0002-4265-1595

REFERENCES

Agangi, A., Hofmann, A., Eickmann, B., & Marin-Carbonne, J. (2019). *Mesoarchaean gold mineralisation in the barberton greenstone belt: A review, the archaean geology of the Kaapvaal Craton, Southern Africa* (pp. 171–184). Cham, Switzerland: Springer.

Agangi, A., Hofmann, A., Eickmann, B., Marin-Carbonne, J., & Reddy, S. M. (2016). An atmospheric source of S in Mesoarchaean structurally-controlled gold mineralisation of the Barberton Greenstone Belt. *Precambrian Research*, *285*, 10–20. https://doi.org/10.1016/j.precamres.2016.09.004

Archer, C., & Vance, D. (2006). Coupled Fe and S isotope evidence for Archean microbial Fe (III) and sulfate reduction. *Geology*, *34*, 153–156. https://doi.org/10.1130/G22067.1

Bassim, N., Scott, K., & Giannuzzi, L. A. (2014). Recent advances in focused ion beam technology and applications. *MRS Bulletin*, *39*, 317–325. https://doi.org/10.1557/mrs.2014.52

Beard, B. L., Johnson, C. M., Cox, L., Sun, H., Nealson, K. H., & Aguilar, C. (1999). Iron isotope biosignatures. *Science*, *285*, 1889–1892. https://doi.org/10.1126/science.285.5435.1889

Berg, J. S., Jézéquel, D., Duverger, A., Lamy, D., Laberty-Robert, C., & Miot, J. (2019). Microbial diversity involved in iron and cryptic sulfur cycling in the ferruginous, low-sulfate waters of Lake Pavin. *PLoS ONE*, *14*, e0212787. https://doi.org/10.1371/journal.pone.0212787

Brasier, M., Green, O., Lindsay, J., & Steele, A. (2004). Earth's oldest (~3.5 Ga) Fossils and the Early Eden hypothesis': Questioning the evidence. *Origins of Life and Evolution of the Biosphere*, *34*, 257–269. https://doi.org/10.1023/B:ORIG.0000009845.62244.d3

Busigny, V., Marin-Carbonne, J., Muller, E., Cartigny, P., Rollion-Bard, C., Assayag, N., & Philippot, P. (2017). Iron and sulfur isotope constraints on redox conditions associated with the 3.2 Ga barite deposits of the Mapepe Formation (Barberton Greenstone Belt, South Africa). *Geochimica Et Cosmochimica Acta*, *210*, 247–266. https://doi.org/10.1016/j.gca.2017.05.002

Busigny, V., Planavsky, N. J., Jézéquel, D., Crowe, S., Louvat, P., Moureau, J., … Lyons, T. W. (2014). Iron isotopes in an Archean ocean analogue. *Geochimica Et Cosmochimica Acta*, *133*, 443–462. https://doi.org/10.1016/j.gca.2014.03.004

Byerly, G. R., Kröner, A., Lowe, D. R., Todt, W., & Walsh, M. M. (1996). Prolonged magmatism and time constraints for sediment deposition in the early Archean Barberton greenstone belt: Evidence from the Upper Onverwacht and Fig Tree groups. *Precambrian Research*, *78*, 125–138. https://doi.org/10.1016/0301-9268(95)00073-9

Canfield, D. (2001). Biogeochemistry of sulfur isotopes. *Reviews in Mineralogy and Geochemistry*, *43*, 607–636. https://doi.org/10.2138/gsrmg.43.1.607

Craddock, P. R., & Dauphas, N. (2011). Iron and carbon isotope evidence for microbial iron respiration throughout the Archean. *Earth and Planetary Science Letters*, *303*, 121–132. https://doi.org/10.1016/j.epsl.2010.12.045

Crosby, H. A., Roden, E. E., Johnson, C. M., & Beard, B. L. (2007). The mechanisms of iron isotope fractionation produced during dissimilatory Fe (III) reduction by Shewanella putrefaciens and Geobacter sulfurreducens. *Geobiology*, *5*, 169–189. https://doi.org/10.1111/j.1472-4669.2007.00103.x

Crowe, S. A., Paris, G., Katsev, S., Jones, C., Kim, S.-T., Zerkle, A. L., … Canfield, D. E. (2014). Sulfate was a trace constituent of Archean seawater. *Science*, *346*, 735–739. https://doi.org/10.1126/science.1258966

Czaja, A. D., Johnson, C. M., Beard, B. L., Eigenbrode, J. L., Freeman, K. H., & Yamaguchi, K. E. (2010). Iron and carbon isotope evidence for ecosystem and environmental diversity in the ~2.7 to 2.5 Ga Hamersley Province, Western Australia. *Earth and Planetary Science Letters*, *292*, 170–180. https://doi.org/10.1016/j.epsl.2010.01.032

Czaja, A. D., Johnson, C. M., Beard, B. L., Roden, E. E., Li, W., & Moorbath, S. (2013). Biological Fe oxidation controlled deposition of banded iron formation in the ca. 3770 Ma Isua Supracrustal Belt (West Greenland). *Earth and Planetary Science Letters*, *363*, 192–203. https://doi.org/10.1016/j.epsl.2012.12.025

Dauphas, N., John, S. G., & Rouxel, O. (2017). Iron isotope systematics. *Reviews in Mineralogy and Geochemistry*, *82*, 415–510. https://doi.org/10.2138/rmg.2017.82.11

de Ronde, C. E., de Wit, M. J., & Spooner, E. T. (1994). Early Archean (> 3.2 Ga) Fe-oxide-rich, hydrothermal discharge vents in the Barberton greenstone belt, South Africa. *Geological Society of America Bulletin*, *106*, 86–104.

Decker, N. B., Byerly, G. R., Stiegler, M. T., Lowe, D. R., & Stefurak, E. (2015). High resolution tephra and U/Pb chronology of the 3.33–3.26 Ga Mendon Formation, Barberton Greenstone Belt, South Africa. *Precambrian Research*, *261*, 54–74. https://doi.org/10.1016/j.precamres.2015.02.003

Ding, T., Valkiers, S., Kipphardt, H., De Bievre, P., Taylor, P., Gonfiantini, R., & Krouse, R. (2001). Calibrated sulfur isotope abundance ratios of three IAEA sulfur isotope reference materials and V-CDT with a reassessment of the atomic weight of sulfur. *Geochimica Et Cosmochimica Acta*, *65*, 2433–2437. https://doi.org/10.1016/S0016-7037(01)00611-1

Drabon, N., Galić, A., Mason, P. R., & Lowe, D. R. (2019). Provenance and tectonic implications of the 3.28–3.23 Ga Fig Tree Group, central Barberton greenstone belt, South Africa. *Precambrian Research*, *325*, 1–19.

Endo, Y., Danielache, S. O., & Ueno, Y. (2019). Total pressure dependence of sulfur mass-independent fractionation by SO2 photolysis. *Geophysical Research Letters*, *46*, 483–491.

Farquhar, J., Bao, H., & Thiemens, M. (2000). Atmospheric influence of Earth's Earliest Sulfur Cycle. *Science*, *289*, 756–758. https://doi.org/10.1126/science.289.5480.756

Farquhar, J., Cliff, J., Zerkle, A. L., Kamyshny, A., Poulton, S. W., Claire, M., … Harms, B. (2013). Pathways for Neoarchean pyrite formation constrained by mass-independent sulfur isotopes. *Proceedings of the National Academy of Sciences*, *110*, 17638–17643. https://doi.org/10.1073/pnas.1218851110

Farquhar, J., Wu, N., Canfield, D. E., & Oduro, H. (2010). Connections between sulfur cycle evolution, sulfur isotopes, sediments, and base metal sulfide deposits. *Economic Geology*, *105*, 509–533. https://doi.org/10.2113/gsecongeo.105.3.509

Fike, D. A., Bradley, A. S., & Rose, C. V. (2015). Rethinking the ancient sulfur cycle. *Annual Review of Earth and Planetary Sciences*, *43*, 593–622. https://doi.org/10.1146/annurev-earth-060313-054802

Flynn, T. M., O'Loughlin, E. J., Mishra, B., DiChristina, T. J., & Kemner, K. M. (2014). Sulfur-mediated electron shuttling during bacterial iron reduction. *Science*, *344*, 1039–1042. https://doi.org/10.1126/science.1252066

Frierdich, A. J., Nebel, O., Beard, B. L., & Johnson, C. M. (2019). Iron isotope exchange and fractionation between hematite (α-Fe2O3) and aqueous Fe(II): A combined three-isotope and reversal-approach to equilibrium study. *Geochimica Et Cosmochimica Acta*, *245*, 207–221. https://doi.org/10.1016/j.gca.2018.10.033

Galić, A., Mason, P. R., Mogollón, J. M., Wolthers, M., Vroon, P. Z., & Whitehouse, M. J. (2016). Pyrite in a sulfate-poor Paleoarchean basin was derived predominantly from elemental sulfur: Evidence from 3.2 Ga sediments in the Barberton Greenstone Belt, Kaapvaal

Craton. *Chemical Geology*. https://doi.org/10.1016/j.chemgeo.2016.12.006

Gomes, M., Fike, D., Bergmann, K., Jones, C., & Knoll, A. (2018). Environmental insights from high-resolution (SIMS) sulfur isotope analyses of sulfides in Proterozoic microbialites with diverse mat textures. *Geobiology*, *16*, 17–34. https://doi.org/10.1111/gbi.12265

Gregory, D. D., Large, R. R., Halpin, J. A., Baturina, E. L., Lyons, T. W., Wu, S., … Bull, S. W. (2015). Trace element content of sedimentary pyrite in black shales. *Economic Geology*, *110*, 1389–1410. https://doi.org/10.2113/econgeo.110.6.1389

Guilbaud, R., Butler, I. B., & Ellam, R. M. (2011). Abiotic pyrite formation produces a large Fe isotope fractionation. *Science*, *332*, 1548–1551. https://doi.org/10.1126/science.1202924

Guy, B., Ono, S., Gutzmer, J., Kaufman, A., Lin, Y., Fogel, M., & Beukes, N. (2012). A multiple sulfur and organic carbon isotope record from non-conglomeratic sedimentary rocks of the Mesoarchean Witwatersrand Supergroup, South Africa. *Precambrian Research*, *216*, 208–231. https://doi.org/10.1016/j.precamres.2012.06.018

Halevy, I. (2013). Production, preservation, and biological processing of mass-independent sulfur isotope fractionation in the Archean surface environment. *Proceedings of the National Academy of Sciences*, *110*, 17644–17649. https://doi.org/10.1073/pnas.1213148110

Harman, C., Pavlov, A., Babikov, D., & Kasting, J. (2018). Chain formation as a mechanism for mass-independent fractionation of sulfur isotopes in the Archean atmosphere. *Earth and Planetary Science Letters*, *496*, 238–247. https://doi.org/10.1016/j.epsl.2018.05.041

Hegyi, S., & Halevy, I. (2019) *Understanding microscale isotopic patterns in pyrite using a two dimensional reaction diffusion model*. AGU Fall Meeting 2019, PP13A-02.

Heimann, A., Johnson, C. M., Beard, B. L., Valley, J. W., Roden, E. E., Spicuzza, M. J., & Beukes, N. J. (2010). Fe, C, and O isotope compositions of banded iron formation carbonates demonstrate a major role for dissimilatory iron reduction in ~2.5 Ga marine environments. *Earth and Planetary Science Letters*, *294*, 8–18. https://doi.org/10.1016/j.epsl.2010.02.015

Hofmann, A. (2005). The geochemistry of sedimentary rocks from the Fig Tree Group, Barberton greenstone belt: Implications for tectonic, hydrothermal and surface processes during mid-Archaean times. *Precambrian Research*, *143*, 23–49. https://doi.org/10.1016/j.precamres.2005.09.005

Hofmann, A., & Bolhar, R. (2007). Carbonaceous cherts in the barberton greenstone belt and their significance for the study of early life in the archean record. *Astrobiology*, *7*, 355–388. https://doi.org/10.1089/ast.2005.0288

Johnson, C. M., & Beard, B. L. (2005). Biogeochemical cycling of iron isotopes. *Science*, *309*, 1025–1027.

Johnson, C. M., Beard, B. L., & Roden, E. E. (2008). The iron isotope fingerprints of redox and biogeochemical cycling in modern and ancient Earth. *Annual Review of Earth and Planetary Sciences*, *36*, 457–493.

Johnson, C. M., Ludois, J. M., Beard, B. L., Beukes, N. J., & Heimann, A. (2013). Iron formation carbonates: Paleoceanographic proxy or recorder of microbial diagenesis? *Geology*, *41*, 1147–1150. https://doi.org/10.1130/G34698.1

Johnston, D. T. (2011). Multiple sulfur isotopes and the evolution of Earth's surface sulfur cycle. *Earth-Science Reviews*, *106*, 161–183. https://doi.org/10.1016/j.earscirev.2011.02.003

Johnston, D. T., Hemingway, J., Gill, B. C., & Halevy, I. (2019). *The information encoded in the isotopic composition of sedimentary sulfide*. AGU Fall Meeting, B11L-2245.

Kamo, S., & Davis, D. (1994). Reassessment of Archean crustal development in the Barberton Mountain Land, South Africa, based on U-Pb dating. *Tectonics*, *13*, 167–192. https://doi.org/10.1029/93TC02254

Konhauser, K. O., Planavsky, N. J., Hardisty, D. S., Robbins, L. J., Warchola, T. J., Haugaard, R., … Johnson, C. M. (2017). Iron formations: A global record of Neoarchaean to Palaeoproterozoic environmental history. *Earth-Science Reviews*, *172*, 140–177. https://doi.org/10.1016/j.earscirev.2017.06.012

Kröner, A., Hegner, E., Wendt, J., & Byerly, G. (1996). The oldest part of the Barberton granitoid-greenstone terrain, South Africa: Evidence for crust formation between 3.5 and 3.7 Ga. *Precambrian Research*, *78*, 105–124. https://doi.org/10.1016/0301-9268(95)00072-0

Labidi, J., Cartigny, P., & Jackson, M. G. (2015). Multiple sulfur isotope composition of oxidized Samoan melts and the implications of a sulfur isotope 'mantle array' in chemical geodynamics. *Earth and Planetary Science Letters*, *417*, 28–39. https://doi.org/10.1016/j.epsl.2015.02.004

Large, R. R., Maslennikov, V. V., Robert, F., Danyushevsky, L. V., & Chang, Z. (2007). Multistage sedimentary and metamorphic origin of pyrite and gold in the Giant Sukhoi Log Deposit, Lena Gold Province, Russia. *Economic Geology*, *102*, 1233–1267. https://doi.org/10.2113/gsecongeo.102.7.1233

Li, Y.-L., Konhauser, K. O., Kappler, A., & Hao, X.-L. (2013). Experimental low-grade alteration of biogenic magnetite indicates microbial involvement in generation of banded iron formations. *Earth and Planetary Science Letters*, *361*, 229–237. https://doi.org/10.1016/j.epsl.2012.10.025

Lonergan, D. J., Jenter, H. L., Coates, J. D., Phillips, E. J., Schmidt, T. M., & Lovley, D. R. (1996). Phylogenetic analysis of dissimilatory Fe(III)-reducing bacteria. *Journal of Bacteriology*, *178*, 2402–2408. https://doi.org/10.1128/JB.178.8.2402-2408.1996

Lovley, D. R. (2002). Dissimilatory metal reduction: From early life to bioremediation. *ASM News*, *68*, 231–237.

Lowe, D. R., & Byerly, G. R. (1999). Stratigraphy of the west-central part of the Barberton Greenstone Belt, South Africa. *Special Papers-Geological Society of America*, *329*, 1–36.

Lowe, D. R., & Byerly, G. R. (2007). An overview of the geology of the Barberton greenstone belt and vicinity: Implications for early crustal development. *Developments in Precambrian Geology*, *15*, 481–526.

Luo, G., Junium, C. K., Kump, L. R., Huang, J., Li, C., Feng, Q., … Xie, S. (2014). Shallow stratification prevailed for ~1700 to ~1300 Ma ocean: Evidence from organic carbon isotopes in the North China Craton. *Earth and Planetary Science Letters*, *400*, 219–232. https://doi.org/10.1016/j.epsl.2014.05.020

Lyons, T. W., Reinhard, C. T., & Planavsky, N. J. J. N. (2014). The rise of oxygen in Earth's early ocean and atmosphere. *Nature*, *506*, 307. https://doi.org/10.1038/nature13068

Mansor, M., & Fantle, M. S. (2019). A novel framework for interpreting pyrite-based Fe isotope records of the past. *Geochimica Et Cosmochimica Acta*, *253*, 39–62. https://doi.org/10.1016/j.gca.2019.03.017

Marin-Carbonne, J., Rollion-Bard, C., Bekker, A., Rouxel, O., Agangi, A., Cavalazzi, B., … McKeegan, K. D. (2014). Coupled Fe and S isotope variations in pyrite nodules from Archean shale. *Earth and Planetary Science Letters*, *392*, 67–79. https://doi.org/10.1016/j.epsl.2014.02.009

Marin-Carbonne, J., Rollion-Bard, C., & Luais, B. (2011). In-situ measurements of iron isotopes by SIMS: MC-ICP-MS intercalibration and application to a magnetite crystal from the Gunflint chert. *Chemical Geology*, *285*, 50–61. https://doi.org/10.1016/j.chemgeo.2011.02.019

Montinaro, A., Strauss, H., Mason, P. R. D., Roerdink, D., Münker, C., Schwarz-Schampera, U., … Peters, M. (2015). Paleoarchean sulfur cycling: Multiple sulfur isotope constraints from the Barberton Greenstone Belt, South Africa. *Precambrian Research*, *267*, 311–322. https://doi.org/10.1016/j.precamres.2015.06.008

Muller, É., Philippot, P., Rollion-Bard, C., Cartigny, P., Assayag, N., Marin-Carbonne, J., … Sarma, D. S. (2017). Primary sulfur isotope signatures preserved in high-grade Archean barite deposits of the Sargur Group, Dharwar Craton, India. *Precambrian Research*, *295*, 38–47. https://doi.org/10.1016/j.precamres.2017.04.029

Nishizawa, M., Maruyama, S., Urabe, T., Takahata, N., & Sano, Y. (2010). Micro-scale (1.5 μm) sulphur isotope analysis of contemporary and

early Archean pyrite. *Rapid Communications in Mass Spectrometry*, *24*, 1397–1404. https://doi.org/10.1002/rcm.4517

Noel, M. (2009). Levée dz log d'une carotte de forage et analyses minéralogiques et isotopiques préliminaires (Formation de Fig Tree, 3.2 Ga Barberton, Afrique du Sud), Master Thesis, Université de Paris, IPGP.

Oduro, H., Harms, B., Sintim, H. O., Kaufman, A. J., Cody, G., & Farquhar, J. (2011). Evidence of magnetic isotope effects during thermochemical sulfate reduction. *Proceedings of the National Academy of Sciences*, *108*, 17635–17638. https://doi.org/10.1073/pnas.1108112108

Ono, S., Wing, B., Johnston, D., Farquhar, J., & Rumble, D. (2006). Mass-dependent fractionation of quadruple stable sulfur isotope system as a new tracer of sulfur biogeochemical cycles. *Geochimica Et Cosmochimica Acta*, *70*, 2238–2252. https://doi.org/10.1016/j.gca.2006.01.022

Peng, X., Zhu, X.-K., Shi, F., Yan, B., Zhang, F., Zhao, N., … Shields, G. A. (2019). A deep marine organic carbon reservoir in the non-glacial Cryogenian ocean (Nanhua Basin, South China) revealed by organic carbon isotopes. *Precambrian Research*, *321*, 212–220. https://doi.org/10.1016/j.precamres.2018.12.013

Philippot, P., Van Kranendonk, M., Van Zuilen, M., Lepot, K., Rividi, N., Teitler, Y., … de Wit, M. (2009). Early traces of life investigations in drilling Archean hydrothermal and sedimentary rocks of the Pilbara Craton, Western Australia and Barberton Greenstone Belt, South Africa. *Comptes Rendus Palevol*, *8*, 649–663. https://doi.org/10.1016/j.crpv.2009.06.006

Philippot, P., Van Zuilen, M., Lepot, K., Thomazo, C., Farquhar, J., & Van Kranendonk, M. J. (2007). Early Archaean microorganisms preferred elemental sulfur, not sulfate. *Science*, *317*, 1534–1537. https://doi.org/10.1126/science.1145861

Philippot, P., Van Zuilen, M., & Rollion-Bard, C. (2012). Variations in atmospheric sulphur chemistry on early Earth linked to volcanic activity. *Nature Geosciences*, *5*, 668–674. https://doi.org/10.1038/ngeo1534

Planavsky, N., Rouxel, O. J., Bekker, A., Hofmann, A., Little, C. T., & Lyons, T. W. (2012). Iron isotope composition of some Archean and Proterozoic iron formations. *Geochimica Et Cosmochimica Acta*, *80*, 158–169. https://doi.org/10.1016/j.gca.2011.12.001

Polyakov, V. B., Osadchii, E. G., Voronin, M. V., Osadchii, V. O., Sipavina, L. V., Chareev, D. A., … Gavrichev, K. S. (2019). Iron and Sulfur Isotope Factors of Pyrite: Data from Experimental Mössbauer Spectroscopy and Heat Capacity. *Geochemistry International*, *57*(4), 369–383.

Raiswell, R., Whaler, K., Dean, S., Coleman, M. L., & Briggs, D. E. G. (1993). A simple three dimensional model of diffusion with precipitation applied to localised pyrite formation in framboids, fossils and detrital iron minerals. *Marine Geology*, *113*, 89–100. https://doi.org/10.1016/0025-3227(93)90151-K

Raven, M. R., Sessions, A. L., Fischer, W. W., & Adkins, J. F. (2016). Sedimentary pyrite δ34S differs from porewater sulfide in Santa Barbara Basin: Proposed role of organic sulfur. *Geochimica Et Cosmochimica Acta*, *186*, 120–134. https://doi.org/10.1016/j.gca.2016.04.037

Rickard, D. (2012). *Sulfidic sediments and sedimentary rocks*. Amsterdam: Newnes.

Rickard, D., & Luther, G. W. (2007). Chemistry of iron sulfides. *Chemical Reviews*, *107*, 514–562. https://doi.org/10.1021/cr0503658

Roerdink, D. L., Mason, P. R., Whitehouse, M. J., & Brouwer, F. M. (2016). Reworking of atmospheric sulfur in a Paleoarchean hydrothermal system at Londozi, Barberton Greenstone Belt, Swaziland. *Precambrian Research*, *280*, 195–204. https://doi.org/10.1016/j.precamres.2016.05.007

Roerdink, D. L., Mason, P. R., Whitehouse, M. J., & Reimer, T. (2013). High-resolution quadruple sulfur isotope analyses of 3.2 Ga pyrite from the Barberton Greenstone Belt in South Africa reveal distinct environmental controls on sulfide isotopic arrays. *Geochimica Et Cosmochimica Acta*, *117*, 203–215. https://doi.org/10.1016/j.gca.2013.04.027

Rolison, J. M., Stirling, C. H., Middag, R., Gault-Ringold, M., George, E., Rijkenberg, M. J. J. E., & Letters, P. S. (2018). Iron isotope fractionation during pyrite formation in a sulfidic Precambrian ocean analogue. *Earth and Planetary Science Letters*, *488*, 1–13. https://doi.org/10.1016/j.epsl.2018.02.006

Rouxel, O. J., Bekker, A., & Edwards, K. J. (2005). Iron isotope constraints on the Archean and Paleoproterozoic ocean redox state. *Science*, *307*, 1088–1091. https://doi.org/10.1126/science.1105692

Rouxel, O., Sholkovitz, E., Charette, M., & Edwards, K. J. (2008). Iron isotope fractionation in subterranean estuaries. *Geochimica et Cosmochimica Acta*, *72*(14), 3413–3430.

Schidlowski, M., Hayes, J., & Kaplan, I. (1983) *Isotopic inferences of ancient biochemistries-Carbon, sulfur, hydrogen, and nitrogen*.

Schiffbauer, J. D., & Xiao, S. (2009). Novel application of focused ion beam electron microscopy (FIB-EM) in preparation and analysis of microfossil ultrastructures: A new view of complexity in early Eukaryotic organisms. *Palaios*, *24*, 616–626. https://doi.org/10.2110/palo.2009.p09-003r

Schopf, J. W., Kudryavtsev, A. B., Czaja, A. D., & Tripathi, A. B. (2007). Evidence of Archean life: Stromatolites and microfossils. *Precambrian Research*, *158*, 141–155. https://doi.org/10.1016/j.precamres.2007.04.009

Severmann, S., Johnson, C. M., Beard, B. L., German, C. R., Edmonds, H. N., Chiba, H., & Green, D. R. H. (2004). The effect of plume processes on the Fe isotope composition of hydrothermally derived Fe in the deep ocean as inferred from the Rainbow vent site, Mid-Atlantic Ridge, 36 14′ N. *Earth and Planetary Science Letters*, *225*(1–2), 63–76.

Shen, Y., Buick, R., & Canfield, D. E. (2001). Isotopic evidence for microbial sulphate reduction in the early Archaean era. *Nature*, *410*, 77–81. https://doi.org/10.1038/35065071

Syverson, D. D., Borrok, D. M., & Seyfried, W. E. Jr (2013). Experimental determination of equilibrium Fe isotopic fractionation between pyrite and dissolved Fe under hydrothermal conditions. *Geochimica et Cosmochimica Acta*, *122*, 170–183.

Thamdrup, B., Finster, K., Hansen, J. W., & Bak, F. (1993). Bacterial disproportionation of elemental sulfur coupled to chemical reduction of iron or manganese. *Applied and Environmental Microbiology*, *59*, 101–108. https://doi.org/10.1128/AEM.59.1.101-108.1993

Thiemens, M. H., & Lin, M. (2019). Use of isotope effects to understand the present and past of the atmosphere and climate and track the origin of life. *Angewandte Chemie International Edition*. https://doi.org/10.1002/ange.201812322

Tice, M. M., Bostick, B. C., & Lowe, D. R. (2004). Thermal history of the 3.5–3.2 Ga Onverwacht and Fig Tree Groups, Barberton greenstone belt, South Africa, inferred by Raman microspectroscopy of carbonaceous material. *Geology*, *32*, 37–40. https://doi.org/10.1130/G19915.1

Tice, M. M., & Lowe, D. R. (2006). The origin of carbonaceous matter in pre-3.0 Ga greenstone terrains: A review and new evidence from the 3.42 Ga Buck Reef Chert. *Earth-Science Reviews*, *76*, 259–300.

Trower, E. J., & Lowe, D. R. (2016). Sedimentology of the ~3.3 Ga upper Mendon Formation, Barberton Greenstone Belt, South Africa. *Precambrian Research*, *281*, 473–494. https://doi.org/10.1016/j.precamres.2016.06.003

Ueno, Y., Ono, S., Rumble, D., & Maruyama, S. (2008). Quadruple sulfur isotope analysis of ca. 3.5Ga Dresser Formation: New evidence for microbial sulfate reduction in the early Archean. *Geochimica Et Cosmochimica Acta*, *72*, 5675–5691. https://doi.org/10.1016/j.gca.2008.08.026

Ueno, Y., Yurimoto, H., Yoshioka, H., Komiya, T., & Maruyama, S. (2002). Ion microprobe analysis of graphite from ca. 3.8 Ga metasediments, Isua supracrustal belt, West Greenland: Relationship between

Metamorphism and Carbon Isotopic Composition. *Geochimica Et Cosmochimica Acta*, *66*, 1257–1268.

van Zuilen, M. A., Chaussidon, M., Rollion-Bard, C., & Marty, B. (2007). Carbonaceous cherts of the Barberton Greenstone Belt, South Africa: Isotopic, chemical and structural characteristics of individual microstructures. *Geochimica Et Cosmochimica Acta*, *71*, 655–669. https://doi.org/10.1016/j.gca.2006.09.029

Vargas, M., Kashefi, K., Blunt-Harris, E. L., & Lovley, D. R. (1998). Microbiological evidence for Fe (III) reduction on early Earth. *Nature*, *395*, 65–67. https://doi.org/10.1038/25720

Viljoen, M., & Viljoen, R. (1970). Archaean vulcanicity and continental evolution in the Barberton region, Transvaal. In T. N. Clifford & I. Gass (Eds.), *African magmatism and tectonics* (pp. 27–39). Edingburgh, UK: Oliver and Boyd.

Walsh, M. W. (1992). Microfossils and possible microfossils from the early archean onverwacht group, Barberton mountain land, South Africa. *Precambrian Research*, *54*, 271–293. https://doi.org/10.1016/0301-9268(92)90074-X

Walsh, M. M., & Lowe, D. R. (1999). Modes of accumulation of carbonaceous matter in the early Archean: A petrographic and geochemical study of the carbonaceous cherts of the Swaziland Supergroup. *Special Papers-Geological Society of America*, 115–132.

Whitehouse, M. J., & Fedo, C. M. (2007). Microscale heterogeneity of Fe isotopes in >3.71 Ga banded iron formation from the Isua Greenstone Belt, southwest Greenland. *Geology*, *35*, 719–722.

Wirth, R. (2009). Focused Ion Beam (FIB) combined with SEM and TEM: Advanced analytical tools for studies of chemical composition, microstructure and crystal structure in geomaterials on a nanometre scale. *Chemical Geology*, *261*, 217–229. https://doi.org/10.1016/j.chemgeo.2008.05.019

Yoshiya, K., Sawaki, Y., Shibuya, T., Yamamoto, S., Komiya, T., Hirata, T., & Maruyama, S. (2015). In-situ iron isotope analyses of pyrites from 3.5 to 3.2 Ga sedimentary rocks of the Barberton Greenstone Belt, Kaapvaal Craton. *Chemical Geology*, *403*, 58–73. https://doi.org/10.1016/j.chemgeo.2015.03.007

Zerkle, A. L., House, C. H., & Brantley, S. L. (2005). Biogeochemical signatures through time as inferred from whole microbial genomes. *American Journal of Science*, *305*, 467–502. https://doi.org/10.2475/ajs.305.6-8.467

Zhelezinskaia, I., Kaufman, A. J., Farquhar, J., & Cliff, J. (2014). Large sulfur isotope fractionations associated with Neoarchean microbial sulfate reduction. *Science*, *346*, 742–744. https://doi.org/10.1126/science.1256211

How to cite this article: Marin-Carbonne J, Busigny V, Miot J, et al. In Situ Fe and S isotope analyses in pyrite from the 3.2 Ga Mendon Formation (Barberton Greenstone Belt, South Africa): Evidence for early microbial iron reduction. *Geobiology*. 2020;18:306–325. https://doi.org/10.1111/gbi.12385